Resurrection of plant disease resistance proteins via helper NLR bioengineering

Mauricio P. Contreras[1], Hsuan Pai[1], Muniyandi Selvaraj[1], AmirAli Toghani[1], David M. Lawson[2], Yasin Tumtas[3], Cian Duggan[3], Enoch Lok Him Yuen[3], Clare E. M. Stevenson[2], Adeline Harant[1], Chih-Hang Wu[4], Tolga O. Bozkurt[3], Sophien Kamoun[1,*] and Lida Derevnina[1,†,*]

1: The Sainsbury Laboratory, University of East Anglia, Norwich, United Kingdom.
2: Department of Biochemistry and Metabolism, John Innes Centre, Norwich, United Kingdom.
3: Department of Life Sciences, Imperial College, London, United Kingdom.
4: Institute of Plant and Microbial Biology, Academia Sinica, Taipei, Taiwan.

†Current address: Crop Science Centre, Department of Plant Sciences, University of Cambridge, Cambridge, United Kingdom.

*Correspondence to: sophien.kamoun@tsl.ac.uk (SK); ld645@cam.ac.uk (LD)

One sentence summary: A helper NLR is mutated to evade inhibition by a parasite effector.

Abstract

Parasites counteract host immunity by suppressing helper NLR proteins that function as central nodes in immune receptor networks. Understanding the mechanisms of immunosuppression can lead to strategies for bioengineering disease resistance. Here, we show that a cyst nematode virulence effector binds and inhibits oligomerization of the helper NLR protein NRC2 by physically preventing intramolecular rearrangements required for activation. A single amino acid polymorphism at the binding interface between NRC2 and the inhibitor is sufficient for this helper NLR to evade immune suppression, thereby restoring the activity of multiple disease resistance genes. This points to a novel strategy for resurrecting disease resistance in crop genomes.

Introduction

The nucleotide binding and leucine-rich repeat (NLR) class of intracellular immune receptors are an important component of innate immunity in plants and animals. They mediate intracellular recognition of pathogens and subsequently initiate an array of immune responses in order to counteract infection (*1, 2*). NLRs can be activated by pathogen-secreted virulence proteins, termed effectors, which pathogens deliver into host cells to modulate host physiology (*2*). A hallmark of plant and animal NLR activation is their oligomerization into higher order immune complexes termed resistosomes or inflammasomes, respectively (*3-9*). These complexes initiate immune signaling via diverse mechanisms, often leading to a form of programmed cell death, termed hypersensitive response (HR) in plants or pyroptosis in animals (*10, 11*). Recent studies have reported NLR-like proteins mediating antiviral immunity and programmed cell death in prokaryotes via mechanisms analogous to those found in eukaryotic NLRs, suggesting that this is a conserved defense mechanism across all three domains of life (*12*). Remarkably, pathogen effectors can act both as triggers and suppressors of NLR-mediated immunity (*13*). In some cases, adapted pathogens deploy effectors which directly or indirectly interfere with NLR signaling to suppress immune activation (*12, 14-17*). However, the exact biochemical mechanisms by which pathogen effectors compromise NLR-mediated immunity to promote disease remain largely unknown. Moreover, whereas multiple strategies to bioengineer novel effector recognition specificities in NLRs have been proposed in recent years (*18*), approaches to mitigate the impact of effector-mediated immune suppression of NLRs are lacking.

NLRs belong to the signal ATPases with numerous domains (STAND) superfamily. They typically exhibit a tripartite domain architecture consisting of an N-terminal signaling domain, a central nucleotide binding domain and C-terminal superstructure forming repeats (*2*). The central domain, termed NB-ARC (nucleotide binding adaptor shared by APAF-1, plant R proteins and CED-4) in plant NLRs, is a hallmark of this protein family and plays a key role as a molecular switch, mediating conformational changes required for activation. NB-ARC domains consist of a nucleotide binding domain (NB), a helical domain (HD1), and a winged-helix domain (WHD) (*2, 19*). Diverse NLR activation and signaling strategies are found in nature. In some cases one NLR protein, termed a singleton, can mediate both elicitor perception and subsequent immune signaling (*20*). However, some NLRs can function as receptor pairs or in higher order configurations termed immune receptor networks (*13, 21*). In these cases, one NLR acts as a pathogen sensor, requiring a second helper NLR to initiate immune signaling. Such is the case in the solanaceous NRC immune receptor network,

62 which is comprised of multiple sensor NLRs that require an array of downstream helper NLRs termed
63 NRCs (NLRs required for cell death) to successfully initiate immune signaling. Upon perception of
64 their cognate effectors, sensors in this network activate oligomerization of their downstream NRC
65 helpers into a putative NRC resistosome, without stably forming part of the mature complex. This
66 has been termed the activation-and release model (*4*). The NRC network can encompass up to half of
67 the NLRome in some solanaceous plant species and plays a key role in mediating immunity against a
68 variety of plant pathogens including oomycetes, bacteria, viruses, nematodes and insects (*15, 21*).
69
70 Plant and metazoan parasites have evolved effectors that interfere with host NLR signaling to promote
71 disease. Parasite effectors can suppress NLR-mediated immunity indirectly by interfering with host
72 proteins that act downstream of NLR signaling (*15, 17, 22, 23*), or directly by interacting with NLRs
73 to inhibit their functions (*15, 16, 24*). One such example is the potato cyst nematode (*Globodera*
74 *rostochiensis*) effector, SPRYSEC15 (SS15), which can suppress signaling mediated by *Nicotiana*
75 *benthamiana* helper NLRs NRC2 and NRC3 and tomato (*Solanum lycopersicum*) helper NLR NRC1, by
76 binding to their central NB-ARC domains (*15*) (**Fig. 1A, Fig. S1A**). In this study, we reasoned that
77 mapping the binding interface between SS15 and its target helper NLRs would enable us to
78 bioengineer NLR variants that evade pathogen suppression, therefore resurrecting the immune
79 signaling activity of upstream sensors in the NRC network.
80

81 **Results**

82 First, we investigated how SS15 binding to NRC2 prevents immune signaling., notably whether SS15
83 prevents oligomerization of NRC following sensor NLR activation. To test this hypothesis, we
84 transiently co-expressed NRC2 or NRC4 with their upstream sensor Rx and the effector SS15 in leaves
85 of *nrc2/3/4* CRISPR KO *N. benthamiana* plants and leveraged previously established BN-PAGE-based
86 readouts for NRC resistosome formation (*4*). For biochemical analyses, we used previously described
87 NRC2 and NRC4 variants with mutations in their N-terminal MADA motifs ($NRC2^{EEE}$ and $NRC4^{AAA}$,
88 respectively) which abolish cell death induction without compromising receptor activation,
89 oligomerization, or localization (*4, 25, 26*). We activated the Rx-NRC system by co-expressing PVX
90 CP-GFP or free GFP as an inactive control. In the absence of SS15, both NRC2 and NRC4
91 oligomerize upon effector-triggered activation mediated by their upstream sensor Rx. However, when
92 SS15 is present, Rx/CP-activated NRC2 is unable to oligomerize and appears as a band of ~240 kDa,
93 which co-migrates with SS15. Inactive NRC2 co-expressed with SS15 also migrates as a band of ~240

94 kDa, which is slower-migrating relative to inactive NRC2 in the absence of SS15, indicative of *in vivo*
95 NRC2-SS15 complex formation (**Fig. 1B, Fig. S1**). We also observed that SS15 co-expression not
96 only blocks NRC2 oligomerization but also prevents the previously reported shift of NRC2 from
97 cytoplasm to PM as well as the formation of NRC2 PM-associated puncta upon Rx/CP activation
98 (**Fig. S2**) (*4*). In contrast, NRC4 oligomerization is not affected in the presence of SS15, which is in
99 line with previous findings that NRC4 immune signaling is not suppressed by SS15 (*15*). We conclude
100 that SS15 can suppress immune signaling by acting as a direct proteinaceous inhibitor of NRC2, but
101 not NRC4, by directly binding to its NB-ARC domain to block the formation of a signal-competent
102 oligomeric resistosome.
103
104 Given that NRC4 retains the capacity to oligomerize in the presence of SS15, we leveraged this
105 differential SS15 sensitivity between NRC2 and NRC4 to identify the domain that determines SS15
106 association and inhibition. We generated a series of NRC2-NRC4 chimeric proteins (**Fig. 2A-2B, Fig.**
107 **S3**), which we subsequently assayed for SS15 association via *in planta* co-immunoprecipitation. We
108 identified one chimeric variant of NRC4, carrying the HD1-1 region of NRC2 ($NRC4^{2HD1-1}$), which
109 gains association to SS15 (**Fig. 2C**). Unlike NRC4, $NRC4^{2HD1-1}$ is susceptible to inhibition by SS15
110 and is unable to oligomerize and trigger cell death in the presence of SS15 (**Fig. 2D-2E, Fig. S3, Fig.**
111 **S4**). We conclude that the HD1-1 region is important for association to SS15 and for the effector to
112 directly inhibit NRC oligomerization and programmed cell death.
113
114 To further define the interface between SS15 and NRC proteins, we crystallized SS15 in complex with
115 the NB-ARC domain of SlNRC1, a tomato NRC that is inhibited by the nematode effector. We
116 subsequently solved the structure using X-ray diffraction data collected to 4.5 Å resolution (**Fig. 3A**,
117 **Fig. S5**, **Table S3**), which allowed us to determine that SS15 binds to a loop in the HD1-1 region of
118 NRCs which connects the NB domain to the HD1 and WHD domains. This provides orthogonal
119 evidence that the SS15-NRC interactions are mediated by this region as shown with the chimera
120 experiments (**Fig. 2**). This loop was previously shown to act as a "hinge", allowing the NB domain to
121 rotate relative to the HD1 and WHD domains following activation (**Fig. S5**, **Movie S1**) (*27*). We
122 propose that SS15 prevents conformational changes that are critical for NLR activation by binding
123 and immobilizing the NB-HD1 hinge.
124

125 Given that SS15 suppresses cell death induction mediated by SlNRC1, NRC2 and NRC3 but not
126 NRC4 or other well characterized NLRs such as ZAR1 (**Fig. S1**) (*15*), we leveraged the high degree
127 of conservation that is characteristic of plant NB-ARC domains to narrow down residues within the
128 binding interface that underpin this interaction. We shortlisted residues within the HD1-1 region that
129 are similar in SlNRC1, NRC2 and NRC3 but different in NRC4 or AtZAR1 (**Fig. 3B**). Combining
130 information from the co-crystal structure and the alignments allowed us to select 13 candidate residues
131 to test by mutagenesis in NRC2 (**Fig. 3B**). We mutated each of these residues to the corresponding
132 amino acid found in NRC4 and screened these NRC2 variants for susceptibility to SS15 inhibition in
133 cell death assays. This revealed two variants, NRC2^{E316P} and NRC2^{D317K} which triggered cell death
134 when activated by Rx/CP and were no longer inhibited by SS15 (**Fig. 3C, Fig. S6, Fig. S7**). We also
135 tested all 13 single amino acid mutants for association with SS15 by *in planta* co-immunoprecipitation
136 and found that NRC2^{E316P} and NRC2^{D317K} exhibited reduced association with SS15 relative to NRC2
137 (**Fig. 3D, Fig. S6**), which is in line with the observation that SS15 is not able to suppress these variants
138 (**Fig. 3C**). We conclude that the E316 and D317 residues are critical for SS15-mediated inhibition of
139 NRC2 and that mutating these residues to their equivalent amino acid in NRC4 allows Rx/CP-
140 activated NRC2 to evade SS15 association and inhibition.
141
142 We next tested whether these two SS15-evading variants of NRC2 could restore functionality of
143 NRC2-dependent sensor NLRs that are suppressed by the parasite effector. We tested this by
144 performing complementation assays with NRC2^{E316P} and NRC2^{D317K} in *nrc2/3/4* CRISPR KO *N.*
145 *benthamiana* plants. We activated the NRC2 variants with a panel of agronomically important sensor
146 NLRs mediating resistance to diverse pathogens, including the potato cyst nematode R gene Gpa2 (an
147 allele of Rx), as well as other well characterized oomycete and bacterial resistance proteins.
148 Remarkably, NRC2^{D317K} evaded SS15 inhibition with all tested sensor NLRs restoring their capacity
149 to activate immune signaling (**Fig 4A**, **Fig. S8, Fig. S9**). In contrast, NRC2^{E316P} could evade SS15
150 suppression when activated by Rx, but not when activated by other sensors. We therefore selected
151 NRC2^{D317K} for follow-up biochemical studies, using BN-PAGE-based assays. Unlike NRC2, activated
152 NRC2^{D317K} oligomerized even in the presence of SS15 and did not form an *in vivo* complex with the
153 inhibitor (**Fig. 4B**). We conclude that NRC2^{D317K} can fully evade SS15-mediated immune suppression,
154 retaining the capacity to oligomerize and mediate cell death when activated by multiple agronomically
155 important sensor NLRs.
156

157 ## Conclusion

158 Our study reveals how a parasite effector has evolved as an inhibitor of a helper NLR by directly
159 binding its NB-ARC domain to prevent resistosome formation and immune signaling. By binding and
160 immobilizing a critical hinge loop in the HD1 region of the NB-ARC, SS15 restricts movement of the
161 NB domain relative to the HD1 and WHD domains, preventing immune receptor activation.
162 Remarkably, while SS15 can bind and inhibit NRC2, it cannot bind or inhibit the NRC2 paralog
163 NRC4. We exploited NRC4's resilience to SS15 inhibition by making chimeric NRC2-NRC4 variants
164 which, together with structural information, helped us identify the inhibitor binding interface.
165 Mutational studies of this interface allowed us to generate a single amino acid variant of NRC2
166 ($NRC2^{D317K}$) that evades SS15 inhibition without compromising receptor signaling capacity. This
167 $NRC2^{D317K}$ variant can now support signaling by any NRC2-dependent sensor even in the presence of
168 SS15.
169
170 The existence of plant parasite secreted NLR inhibitors suggests that suppressed resistance genes may
171 occur in crop genomes. Leveraging the approach detailed in this study, it may be possible to resurrect
172 cryptic or defeated resistance proteins to enhance disease resistance. Moreover, considering that
173 multiple sensors can signal through the same downstream helper, applying this approach to helper
174 NLRs holds potential to simultaneously resurrect multiple upstream sensor NLRs. Importantly, the
175 single amino acid NRC2 variants we identified could in theory be generated in-locus using gene editing
176 technologies in agronomically important crop species, making deployment of this technology viable
177 in countries where transgenic approaches are not feasible. Our work describes a novel approach to
178 achieve robust immunity by engineering NLRs that avoid parasite suppression. This could in theory
179 be applied to other plant, metazoan or even prokaryotic NLR immune receptors that are directly
180 targeted by parasite effectors (*12, 15, 16, 24*). Combined with recent advances in NLR engineering to
181 achieve novel pathogen recognition specificities (*18, 28*), this technology holds the potential to unlock
182 a new era in disease resistance breeding.
183

184 ## Materials and Methods

185 **Plant growth conditions**

186 Wild-type and *nrc2/3/4* CRISPR mutant *Nicotiana benthamiana* lines were grown in a controlled
187 environment growth chamber with a temperature range of 22 to 25 ºC, humidity of 45% to 65% and
188 a 16/8-hour light/dark cycle.

189

190 **Plasmid construction**

191 We used the Golden Gate Modular Cloning (MoClo) kit (*29*) and the MoClo plants part kit (*30*) for
192 cloning. All vectors used were generated with these kits unless otherwise stated. Cloning design and
193 sequence analysis were done using Geneious Prime (v2021.2.2; https://www.geneious.com). Plasmid
194 construction is described in more detail in **Table S1**.

195

196 **Cell death assays by agroinfiltration**

197 Proteins of interest were transiently expressed in *N. benthamiana* according to previously described
198 methods (*31*). Briefly, leaves from 4–5-week-old plants were infiltrated with suspensions
199 of *Agrobacterium tumefaciens* GV3101 pM90 strains transformed with expression vectors coding for
200 different proteins indicated. Final OD_{600} of all *A. tumefaciens* suspensions were adjusted in infiltration
201 buffer (10 mM MES, 10 mM $MgCl_2$, and 150 µM acetosyringone (pH 5.6)). Final OD_{600} used for each
202 construct is described in **Table S2**.

203

204 **Extraction of total proteins for BN-PAGE and SDS-PAGE assays**

205 Four to five-week-old *N. benthamiana* plants were agroinfiltrated as described above with constructs
206 of interest and leaf tissue was collected 3 days post agroinfiltration for NRC2 and 2 days post
207 agroinfiltration for NRC4. Final OD_{600} used for each construct is described in **Table S2**. BN-PAGE
208 was performed using the Bis-Tris Native PAGE system (Invitrogen) according to the manufacturer's
209 instructions, as described previously (*31*). Leaf tissue was ground using a Geno/Grinder tissue
210 homogenizer. For NRC2, GTMN extraction buffer was used (10% glycerol, 50 mM Tris-HCl (pH
211 7.5), 5 mM $MgCl_2$ and 50 mM NaCl) supplemented with 10 mM DTT, 1x protease inhibitor cocktail
212 (SIGMA) and 0.2% Nonidet P-40 Substitute (SIGMA). For NRC4, GHMN buffer (10% glycerol, 50
213 mM HEPES (pH 7.4), 5 mM $MgCl_2$ and 50 mM NaCl) buffer supplemented with 10mM DTT, 1x
214 protease inhibitor cocktail (SIGMA) and 1% Digitonin (SIGMA) was used for extraction. Samples
215 were incubated in extraction buffer on ice for 10 minutes with short vortex mixing every 2 minutes.

216 Following incubation, samples were centrifuged at 5,000 x*g* for 15 minutes and the supernatant was
217 used for BN-PAGE and SDS-PAGE assays.
218
219 **BN-PAGE assays**
220 For BN-PAGE, samples extracted as detailed above were diluted as per the manufacturer's
221 instructions by adding NativePAGE 5% G-250 sample additive, 4x Sample Buffer and water. After
222 dilution, samples were loaded and run on Native PAGE 3%-12% Bis-Tris gels alongside either
223 NativeMark unstained protein standard (Invitrogen) or SERVA Native Marker (SERVA). The
224 proteins were then transferred to polyvinylidene difluoride membranes using NuPAGE Transfer
225 Buffer using a Trans-Blot Turbo Transfer System (Bio-Rad) as per the manufacturer's instructions.
226 Proteins were fixed to the membranes by incubating with 8% acetic acid for 15 minutes, washed with
227 water and left to dry. Membranes were subsequently re-activated with methanol to correctly visualize
228 the unstained native protein marker. Membranes were immunoblotted as described below.
229
230 **SDS-PAGE assays**
231 For SDS-PAGE, samples were diluted in SDS loading dye and denatured at 72 ºC for 10 minutes.
232 Denatured samples were spun down at 5,000 x*g* for 3 minutes and supernatant was run on 4%-20%
233 Bio-Rad 4%-20% Mini-PROTEAN TGX gels alongside a PageRuler Plus prestained protein ladder
234 (Thermo Scientific). The proteins were then transferred to polyvinylidene difluoride membranes using
235 Trans-Blot Turbo Transfer Buffer using a Trans-Blot Turbo Transfer System (Bio-Rad) as per the
236 manufacturer's instructions. Membranes were immunoblotted as described below.
237
238 **Immunoblotting and detection of BN-PAGE and SDS-PAGE assays**
239 Blotted membranes were blocked with 5% milk in Tris-buffered saline plus 0.01% Tween 20 (TBS-T)
240 for an hour at room temperature and subsequently incubated with desired antibodies at 4 ºC overnight.
241 Antibodies used were anti-GFP (B-2) HRP (Santa Cruz Biotechnology), anti-HA (3F10) HRP
242 (Roche), anti-Myc (9E10) HRP (Roche), and anti-V5 (V2260) HRP (Roche), all used in a 1:5000
243 dilution in 5% milk in TBS-T. To visualize proteins, we used Pierce ECL Western (32106, Thermo
244 Fisher Scientific), supplementing with up to 50% SuperSignal West Femto Maximum Sensitivity
245 Substrate (34095, Thermo Fishes Scientific) when necessary. Membrane imaging was carried out with
246 an ImageQuant LAS 4000 or an ImageQuant 800 luminescent imager (GE Healthcare Life Sciences,
247 Piscataway, NJ). Rubisco loading control was stained using Ponceau S (Sigma).

248 **Co-Immunoprecipitation assays**

249 CoIP assays were performed as described previously (*32*). Total soluble protein was extracted as
250 described above from leaves of *N. benthamiana* 3 days post agro-infiltration using GTEN buffer
251 (10% Glycerol, 25 mM Tris-HCl (pH 7.5), 1mM EDTA, 150 mM NaCl) supplemented with 2%
252 (w/v) polyvinylpolypyrrolidone, 10 mM DTT and 1x protease inhibitor cocktail (SIGMA), 0.3%
253 IGEPAL (SIGMA). OD_{600} used can be found in **Table S2**. Protein extracts were filtered using
254 Minisart 0.45 µm filter (Sartorius Stedim Biotech, Goettingen, Germany). Part of the extract was set
255 aside prior to immunoprecipitation and used for SDS-PAGE as described above. These were the
256 inputs. 1.4 ml of the remaining filtered total protein extract was mixed with 30 µl of anti-c-Myc
257 agarose beads (A7470, SIGMA) and incubated end over end for 90 minutes at 4 ºC. Beads were
258 washed 5 times with immunoprecipitation wash buffer (GTEN extraction buffer with 0.3% v/v
259 IGEPAL (SIGMA)) and resuspended in 60 µl of SDS loading dye. Proteins were eluted from beads
260 by heating for 10 minutes at 72 ºC. Immunoprecipitated samples were used for SDS-PAGE and
261 immunoblotted as described above and compared to the inputs.

262

263 **Confocal microscopy**

264 Three to four-week-old plants were agroinfiltrated as described above with constructs of interest. Final
265 OD_{600} used for each construct is described in **Table S2**. Leaf tissue was prepared for imaging by
266 sectioning of desired area surrounding an infiltration spot using a cork borer size 4, and were mounted,
267 live, in wells containing dH2O made in Carolina Observation Gel to enable diffusion of gasses. The
268 abaxial of the leaf tissue was imaged using a Leica SP8 with 40x water immersion objective. Laser
269 excitations for fluorescent proteins were used as described previously (*33*), namely 488 nm (Argon)
270 for GFP, 561/594 nm (Diode) for RFP and 405 nm (Diode) for BFP.

271

272 **Membrane enrichment assays**

273 Membrane enrichment was carried out by slightly modifying a previously described protocol (*34*). In
274 brief, leaf material was ground to fine powder using liquid nitrogen and 2x volume of extraction buffer
275 was added. Extraction buffer consisted of 0.81M sucrose, 5% (v/v) glycerol, 10 mM EDTA, 10 mM
276 EGTA, 5mM KCl, and 100 mM Tris-HCl (pH 7.5) supplemented with 5 mM DTT, 1% Sigma Plant
277 Protease Inhibitor Cocktail, 1 mM PMSF and 0.5% PVPP. After addition of the buffer, the samples
278 were vortexed for a minute and the cell debris was cleared out by two subsequent centrifugation steps
279 at 1000 xg for 5 min. The supernatant was diluted 1:1 using distilled water and an aliquot of the

280 supernatant was separated as the total fraction (T). The remaining supernatant (200-300 μL) was
281 further centrifuged at 21,000 xg for 90 min at 4°C. This centrifugation yielded the supernatant (soluble
282 fraction, S) and membrane enriched pellet (membrane fraction, M). After separating the soluble
283 fraction, the pellet was resuspended in diluted extraction buffer (without PVPP). All the fractions were
284 diluted with SDS loading dye, and proteins were denatured by incubating at 50°C for 15 min. Western
285 blotting was performed as previously described following SDS-PAGE. Endogenous plasma
286 membrane ATPase was detected using anti-H+ATPase (AS07 260) antibody (Agrisera) as a marker to
287 show the success of membrane enrichment.
288
289 **Heterologous protein production and purification from *E. coli***
290 Heterologous production and purification of SS15 was performed as previously described (*32*).
291 Recombinant SS15 protein (lacking signal peptide) was expressed by cloning in pOPIN-S3C plasmid,
292 with an N-terminal tandem 6xHis-SUMO followed by a 3C protease cleavage site. pOPIN-S3C:SS15
293 was transformed into *E. coli* SHuffle cells. 8L of these cells were grown at 30 ºC in autoinduction
294 media (*35*) to an OD600 of 0.6 to 0.8 followed by overnight incubation at 18 ºC and harvested by
295 centrifugation. Pelleted cells were resuspended in 50 mM Tris HCl (pH 8), 500 mM NaCl, 50 mM
296 Glycine, 5% (vol/vol) glycerol and 20 mM imidazole (buffer A) supplemented with cOmplete EDTA-
297 free protease inhibitor tablets (Roche) and lysed by sonication. The clarified cell lysate was applied to
298 a Ni^{2+}-NTA column connected to an AKTA pure system. 6xHis-SUMO-SS15 was step eluted with
299 elution buffer (buffer A with 500 mM imidazole) and directly injected onto a Superdex 200 26/600
300 gel filtration column pre-equilibrated with buffer B (20 mM HEPES (pH 7.5), 150 mM NaCl). The
301 fractions containing 6xHis-SUMO-SS15 were pooled, and the N-terminal 6xHis-SUMO tag was
302 cleaved by addition of 3C protease (10 μg/mg of fusion protein), incubating overnight at 4ºC. Cleaved
303 SS15 was further purified using a Ni^{2+}-NTA column, this time collecting the flow through to separate
304 the cleaved tag from the SS15 protein. Un-tagged SS15 was further purified by another round of gel
305 filtration as described above. The concentration of protein was judged by absorbance at 280 nm (using
306 a calculated molar extinction coefficient of 35920 M^{-1cm-1} for SS15).
307
308 Heterologous production and purification of $SlNRC1^{NB-ARC}$ was performed as previously described
309 (*36*). Recombinant $SlNRC1^{NB-ARC}$ protein was also expressed cloning in pOPIN-S3C plasmid as
310 described above. pOPIN-S3C:$SlNRC1^{NB-ARC}$ was transformed into *E. coli* Lemo21 (DE3) cells. 8L of
311 these cells were grown at 37 ºC in autoinduction media (*35*) to an OD600 of 0.6 to 0.8 followed by

312 overnight incubation at 18 ºC and harvested by centrifugation. Pelleted cells were resuspended in 50
313 mM Tris HCl (pH 8), 500 mM NaCl, 50 mM Glycine, 5% (vol/vol) glycerol and 20 mM imidazole
314 (buffer A) supplemented with cOmplete EDTA-free protease inhibitor tablets (Roche) and lysed by
315 sonication. The clarified cell lysate was applied to a Ni^{2+}-NTA column connected to an AKTA pure
316 system. 6xHis-SUMO-SlNRC1^{NB-ARC} was step eluted with elution buffer (buffer A with 500 mM
317 imidazole) and directly injected onto a Superdex 200 26/600 gel filtration column pre-equilibrated
318 with buffer B (20 mM HEPES (pH 7.5), 150 mM NaCl). The fractions containing 6xHis-SUMO-
319 SlNRC1^{NB-ARC} were pooled, and the N-terminal 6xHis-SUMO tag was cleaved by addition of 3C
320 protease (10 μg/mg of fusion protein), incubating overnight at 4ºC. Cleaved SlNRC1^{NB-ARC} was further
321 purified using a Ni^{2+}-NTA column, this time collecting the flow through to separate the cleaved tag
322 from the SlNRC1^{NB-ARC} protein. Un-tagged SlNRC1^{NB-ARC} was further purified by another round of gel
323 filtration as described above. The concentration of protein was judged by absorbance at 280 nm (using
324 a calculated molar extinction coefficient of 63370 M^{-1cm-1} for SlNRC1^{NB-ARC}).
325
326 To obtain SlNRC1^{NB-ARC} in complex with SS15, both proteins were incubated in a 1:1 molar ratio
327 overnight at 4 ºC and subjected to gel filtration on a Superdex 200 26/600 gel filtration column as
328 described above. The fractions containing SlNRC1^{NB-ARC} in complex with SS15 were pooled,
329 concentrated to 10-15 mg/ml and subsequently used for crystallisation screens.
330
331 **Crystallisation, data collection, and structure solution**
332 Crystallisation screens were performed at 18°C using the sitting-drop vapour diffusion technique.
333 Drops composed of 0.3 μL of protein solution and 0.3 μL of reservoir solution were set up in MRC
334 96-well crystallisation plates (Molecular Dimensions), which were dispensed using an Oryx Nano or
335 an Oryx8 robot (Douglas Instruments). Crystal growth was monitored using a Minstrel Desktop
336 Crystal Imaging System (Rikagu). Suitable crystals grew after 72 hrs in a Morpheus screen
337 crystallisation condition containing 0.1M MES buffer (pH 6.5), 10% (w/v) PEG8000 and 20% (v/v)
338 ethylene glycol (Molecular Dimensions) and were harvested by flash-cooling in liquid nitrogen using
339 LithoLoops (Molecular Dimensions). X-ray diffraction data were collected at the Diamond Light
340 Source (Didcot, UK) on beamline I03 using an Eiger2 XE 16M pixel array detector (Dectris) with
341 crystals maintained at 100 K by a Cryojet cryocooler (Oxford Instruments).
342 X-ray data were integrated, and scaled using XDS (*37*), as implemented through the XIA2 (*38*)
343 pipeline, and then merged using AIMLESS (*39*), via the CCP4i2 graphical user interface (*40*). The

344 NRC1$^{NB\text{-}ARC}$-SS15 complex crystallised in space group $P6_1$ with cell parameters a=b=128.6, c=170.7 Å,
345 and the best crystal yielded diffraction data to 4.5 Å resolution (see **Table S3** for a summary of data
346 collection and refinement statistics). Given the small size of the dataset, we assigned 10% of the data
347 (883 unique reflections) for the R_{free} calculation, to give a more statistically meaningful metric. The
348 crystal structure of NRC1$^{NB\text{-}ARC}$ alone was already available (PDB 6S2P), but there was no
349 experimentally determined structure for SS15. Thus, we made use of AlphaFold2-multimer (*41*), as
350 implemented through Colabfold
351 (https://colab.research.google.com/github/sokrypton/ColabFold/blob/main/AlphaFold2.ipynb)
352 (*42*) to generate structural predictions for the complex. There was very good sequence coverage for
353 both proteins and the five independent models of the individual components were closely similar. The
354 pLDDT scores were generally good (e.g. averages of 82 and 75 for NRC1$^{NB\text{-}ARC}$ and SS15 models,
355 respectively, from the rank 1 predictions). However, the relative placement of the two components
356 varied across the five models and the corresponding PAE scores indicated very low confidence in
357 these predictions. A comparison of the five NRC1$^{NB\text{-}ARC}$ models with the known crystal structure
358 showed a good agreement (e.g. superposition of the rank 1 model gave an rmsd of 1.77 Å). Given that
359 the AlphaFold2 (AF2) model provided starting coordinates for several loops missing from the crystal
360 structure, we decided to use this model in molecular replacement. Templates for both components
361 were prepared using the "Process Predicted Models" CCP4i2 task, which removed low confidence
362 regions (based on pLDDT) and converted the pLDDT scores in the *B*-factor field of the PDB
363 coordinate files to pseudo *B*-factors. Analysis of the likely composition of the asymmetric unit (ASU)
364 suggested that it contained two copies of each component, giving an estimated solvent content of
365 ~67%. PHASER (*43*) was able to place the four chains within the ASU, although the second SS15
366 domain required manual repositioning with respect to its neighbouring NRC1 domain in order to
367 avoid a number of clashes and improve the fit to the density. This was achieved using COOT (*44*)
368 and guided by the arrangement of the other NRC1-SS15 complex (**Fig. S4**). The structure was then
369 subjected to jelly body refinement in REFMAC5 (*45*) using ProSMART restraints (*46*) generated from
370 the AF2 models, giving R_{work} and R_{free} values of 0.357 and 0.401, respectively, to 4.5 Å resolution.
371
372 Now it was possible to generate more complete models for the components by superposing the
373 original unprocessed AF2 models and trimming these with reference to the improved electron density.
374 Furthermore, a significant region of positive difference density was present at the cores of both NRC1
375 domains, which corresponded to the ADP in the crystal structure; thus we incorporated ADP into the

376 model. Due to the low resolution of the dataset, only very limited rebuilding was possible in COOT,
377 where Geman-McClure and Ramachandran restraints were used to maintain good stereochemical
378 parameters. After several cycles of restrained refinement in REFMAC5 and editing in COOT, a
379 reasonable model was obtained with R_{work} and R_{free} values of 0.258 and 0.298, respectively. However,
380 there remained a region of positive difference density near the N-termini of both SS15 domains that
381 we could not adequately explain. At this point we re-ran the AlphaFold2-multimer predictions, but
382 this time with one copy of the complex taken from the crystal structure as a reference template.
383 Although the new predictions did not produce complexes that were consistent with the X-ray data,
384 and the models for the individual components did not appear to be noticeably improved based on
385 pLDDT scores, we used them as starting points to rebuild the X-ray structure.
386
387 Significantly, for several models, the N-terminal region of SS15 adopted conformations that partially
388 accounted for the region of positive difference density electron density, and this could be improved
389 by careful rebuilding and refinement. This "AlphaFold recycling" procedure was repeated a further
390 two times before finalising the structure, which included residues 153-494 for SlNRC1 (numbered
391 with respect to full length protein) and residues 18-223 for SS15, where residues 33-43 in both copies
392 of the latter formed α-helices that occupied the regions of positive difference density observed earlier.
393 For the last refinement in REFMAC5, the following options were used: ProSMART restraints
394 generated from the latest AF2 models, overall *B*-factor refinement with TLS restraints (where each
395 protein chain was treated as a separate domain), and non-crystallographic symmetry restraints. The
396 final model gave R_{work} and R_{free} values of 0.237 and 0.275, respectively, to 4.5 Å resolution (see **Table**
397 **S3** for a summary of refinement statistics). All structural figures were prepared using ChimeraX (*47*)
398 and PyMOL (*48*).
399

400 **Figures:**

401 **Figure 1**

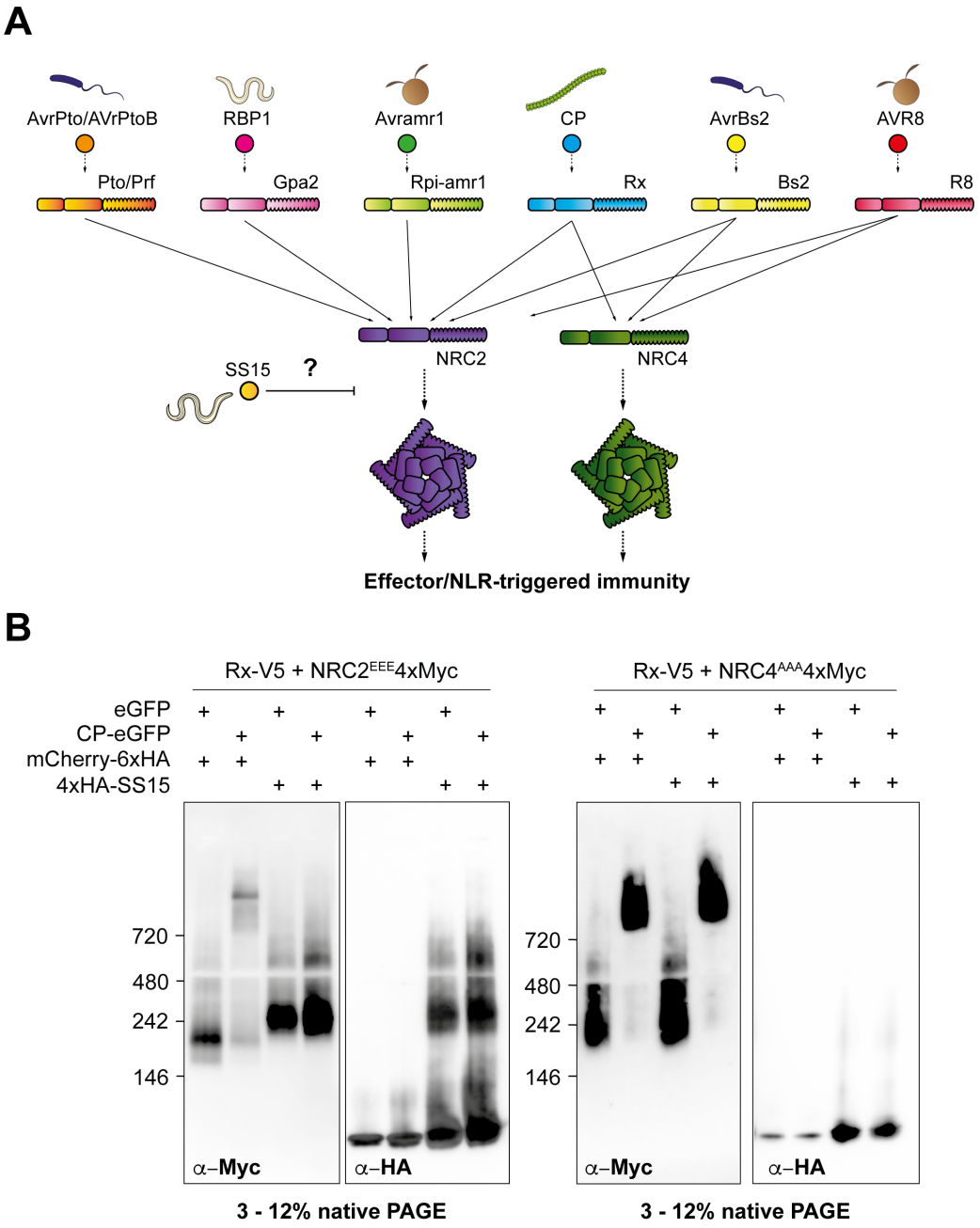

402

403 **Fig. 1: SS15 directly inhibits NRC2, but not NRC4 oligomerization.**

404 (**A**) Schematic representation of the NRC immune receptor network, consisting of multiple sensor
405 NLRs (in blue) and their downstream helper NLRs, NRC2 and NRC4 (in purple and green,
406 respectively). Effector-triggered activation of a sensor leads to downstream helper oligomerization
407 and resistosome formation. The *G. rostochiensis* effector SS15 (in yellow) can directly bind to the NB-

408 ARC domain of NRC2 but not NRC4, thereby inhibiting signaling by directly binding to the NB-ARC
409 domain of this helper NLR. (**B**) BN-PAGE assays with inactive and activated Rx together with NRC2
410 or NRC4, in the absence or presence of SS15. C-terminally V5-tagged Rx and C-terminally 4xMyc-
411 tagged $NRC2^{EEE}$ or $NRC4^{AAA}$ were co-expressed with either free GFP or C-terminally GFP-tagged
412 PVX CP. These effector-sensor-helper combinations were co-infiltrated together with a 6xHA-
413 mCherry fusion protein or with N-terminally 6xHA-tagged SS15. Total protein extracts were run in
414 parallel on native and denaturing PAGE assays and immunoblotted with the appropriate antisera
415 labelled below. Approximate molecular weights (kDa) of the proteins are shown on the left.
416 Corresponding SDS-PAGE assays can be found in **Fig. S1**. The experiment was repeated three times
417 with similar results.
418

419 **Figure 2**

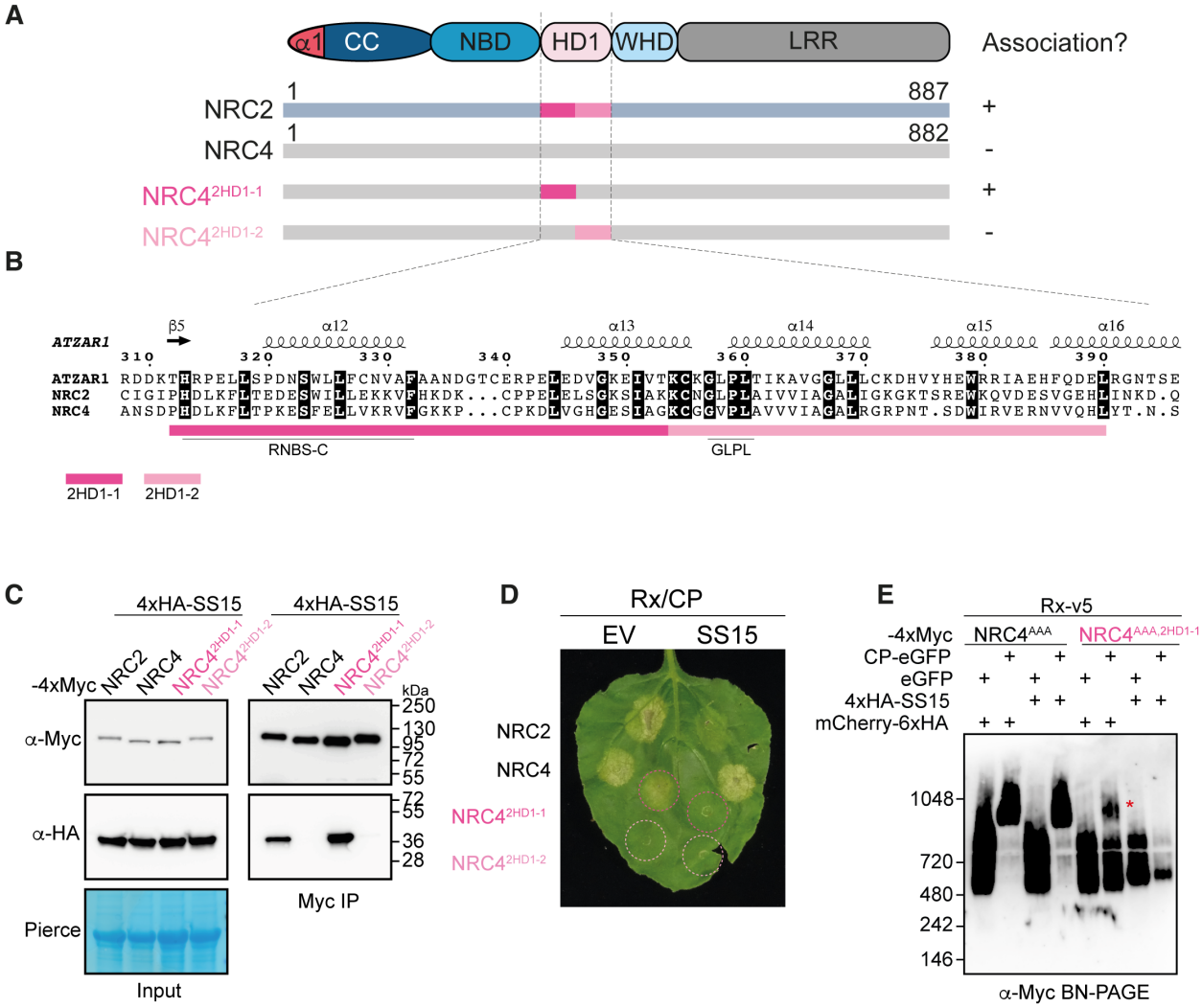

420

421 **Fig. 2: The HD1-1 region of NRC NB-ARC domains determines sensitivity to SS15.**

422 **(A)** Schematic representation of NRC domain architecture, highlighting regions within the NB-ARC
423 domain swapped between NRC2-NRC4 chimeric proteins, namely NRC4^{2HD1-1} and NRC4^{2HD1-2}.
424 Association (+) or lack thereof (-) between these NLR immune receptors and SS15 determined by *in*
425 *planta* co-immunoprecipitation is detailed on the right. (**B**) Close-up view of amino acid sequence
426 alignment between AtZAR1, NRC2 and NRC4 focused on the HD1 region of NB-ARC domain.
427 Predicted secondary structure is shown above the alignment. Well-characterized motifs within this
428 region, such as RNBS-C and GLPL are underlined below the alignment. (**C**) Co-Immunoprecipitation
429 (Co-IP) assays between SS15 and chimeric NRC2-NRC4 variants. C-terminally 4xMyc-tagged NRC
430 proteins were transiently co-expressed with N-terminally 4xHA-tagged SS15. IPs were performed with
431 agarose beads conjugated to Myc antibodies (Myc IP). Total protein extracts were immunoblotted

432 with the appropriate antisera labelled on the left. Approximate molecular weights (kDa) of the proteins
433 are shown on the right. Rubisco loading control was carried out using Ponceau stain (PS). The
434 experiment was repeated three times with similar results. (**D**) Photo of representative leaves from *N.*
435 *benthamiana nrc2/3/4* KO plants showing HR after co-expression of Rx and PVX CP with NRC2,
436 NRC4 and the two NRC2-NRC4 chimeras, $NRC4^{2HD1-1}$ and $NRC4^{2HD1-2}$. These effector-sensor-helper
437 combinations were co-expressed with a free mCherry-6xHA fusion protein (EV) or with N-terminally
438 4xHA-tagged SS15. The experiment consisted of 3 biological replicates with at least 6 technical
439 replicates each. A quantitative analysis of the HR phenotypes can be found in **Fig. S4**. (**E**) BN-PAGE
440 assay with inactive and activated Rx together with NRC4 or an NRC2-NRC4 chimeric protein in the
441 absence or presence of SS15. C-terminally V5-tagged Rx and C-terminally 4xMyc-tagged $NRC4^{AAA}$ or
442 $NRC4^{AAA-2HD1-1}$ were co-expressed with either free GFP or C-terminally GFP-tagged PVX CP. These
443 effector-sensor-helper combinations were co-infiltrated together with a mCherry-6xHA fusion protein
444 or with N-terminally 4xHA-tagged SS15. Total protein extracts were run in parallel on native and
445 denaturing PAGE assays and immunoblotted with the appropriate antisera labelled on the left.
446 Corresponding SDS-PAGE blots can be found in **Fig. S3**. Approximate molecular weights (kDa) of
447 the proteins are shown on the left. The experiment was repeated three times with similar results.
448

449 **Figure 3**

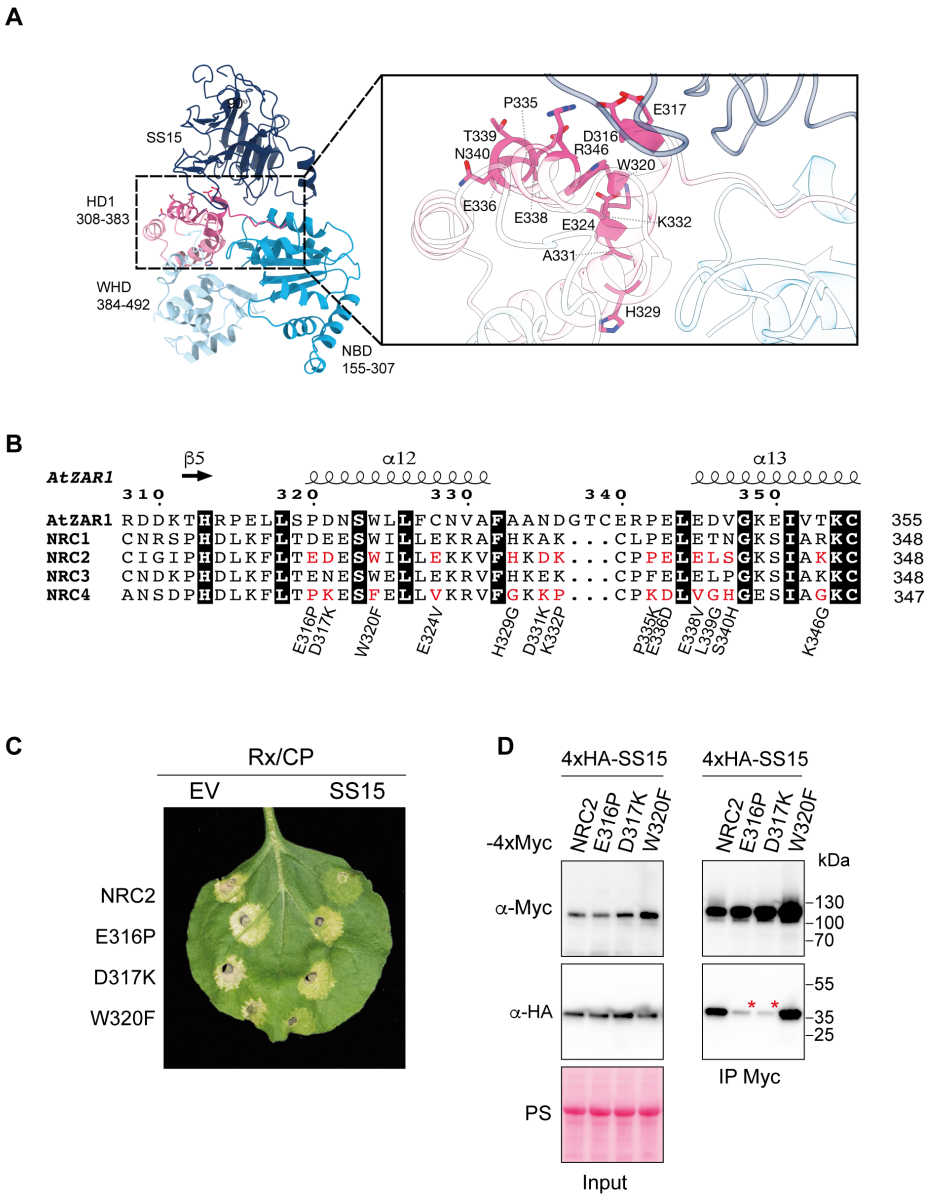

450

451 **Fig. 3: SS15-NRC binding interface enables bioengineering NRC2 variants that evade**
452 **suppression. (A)** Crystal structure of the SS15-SlNRC1^{NB-ARC} complex. The NB, HD1 and WHD
453 domains of SlNRC1^{NB-ARC} are shown in cyan, pale blue and magenta, respectively; SS15 is in dark blue.
454 The inset displays a close-up of the interface between SS15 and the HD1 domain of SlNRC1^{NB-ARC}
455 with the residues corresponding to those selected for mutagenesis in NRC2 highlighted in stick
456 representation. See **Table S3** for a summary of data collection and processing statistics. (**B**) Alignment
457 of HD1-1 region of AtZAR1, SlNRC1, NRC2, NRC3, and NRC4. Candidate residues (highlighted in
458 red) were shortlisted based on the interface identified in the co-crystal structure of SS15 and the

459 SlNRC1 NB-ARC domain, as well as being conserved in SlNRC1, NRC2 and NRC3 but not NRC4
460 and AtZAR1. 13 NRC2 variants were generated by mutating individual candidate positions to the
461 corresponding amino acid in NRC4 (detailed underneath the alignment). (**C**) Photo of representative
462 leaves from *N. benthamiana nrc2/3/4* KO plants showing HR after co-expression of Rx and PVX CP
463 with NRC2, or different NRC2 variants generated. These effector-sensor-helper combinations were
464 co-expressed with a free mCherry-6xHA fusion protein (EV) or with N-terminally 4xHA-tagged SS15.
465 The experiment consisted of 3 biological replicates. A quantitative analysis of HR phenotypes can be
466 found in **Fig. S7**. (**D**) Co-Immunoprecipitation (Co-IP) assays between SS15 and NRC2 variants. C-
467 terminally 4xMyc-tagged NRC2 variants were transiently co-expressed with N-terminally 4xHA-
468 tagged SS15. IPs were performed with agarose beads conjugated to Myc antibodies (Myc IP). While
469 only data for E316P, D317K and W320F NRC2 variants is shown, additional variants were also tested
470 and can be found in **Fig S6**. Total protein extracts were immunoblotted with appropriate antisera
471 labelled on the left. Approximate molecular weights (kDa) of the proteins are shown on the right.
472 Rubisco loading control was carried out using Ponceau stain (PS). The experiment was repeated three
473 times with similar results.
474

475

476 **Figure 4**

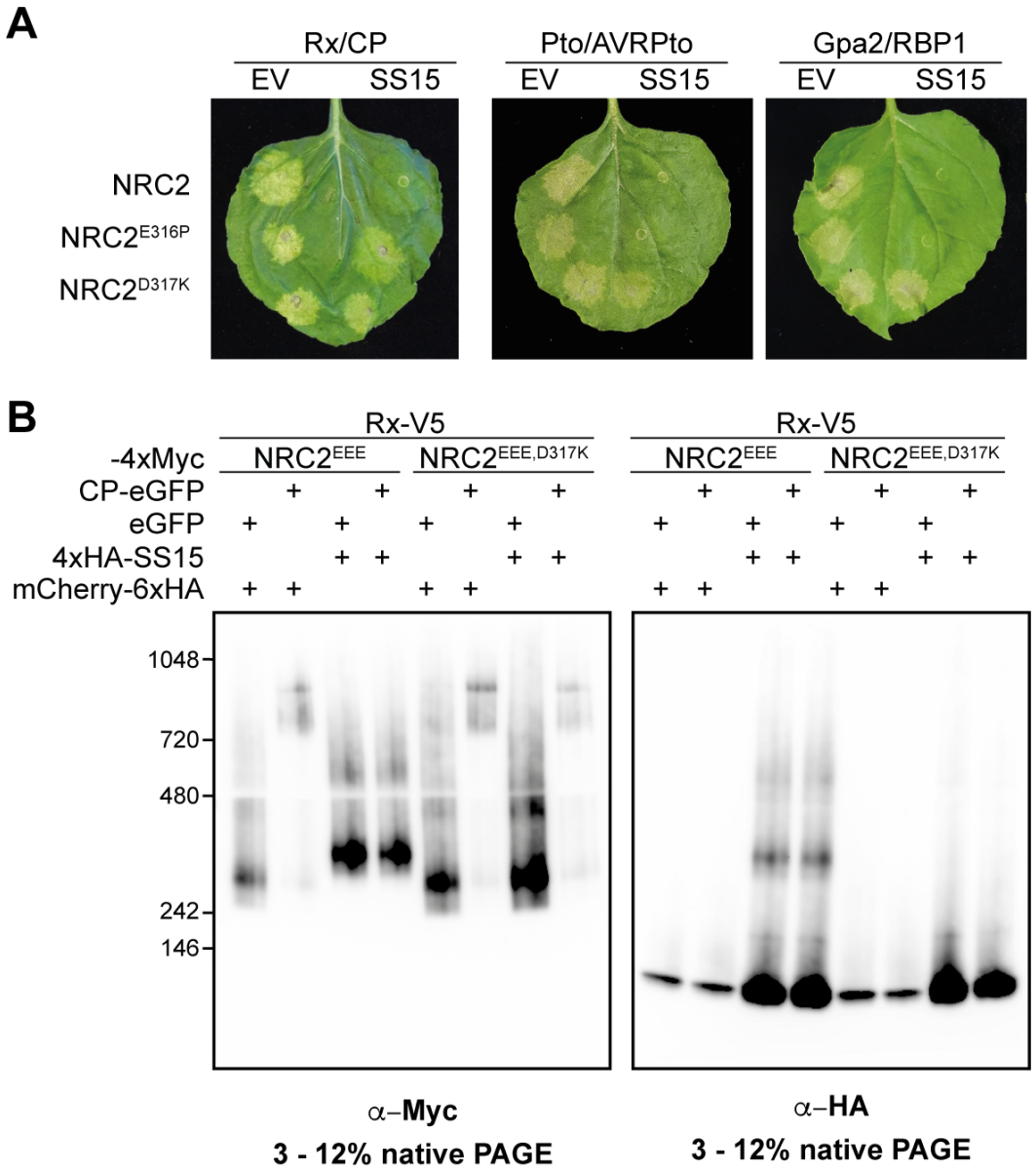

477

478 **Fig. 4: NRC2^{D317K} helper restores immune signaling of multiple disease resistance genes in**
479 **the presence of the effector SS15. (A)** Photo of representative leaves from *N. benthamiana nrc2/3/4*
480 KO plants showing HR after co-expression of Rx/CP, Pto/AVRPto or Gpa2/RBP1 together with
481 NRC2, NRC2^{E316P} or NRC2^{D317K} in the absence or presence of SS15. The experiment consisted of 3
482 biological replicates. A quantitative analysis of HR phenotypes can be found in **Fig. S8**. (**B**) BN-
483 PAGE assays with inactive and activated Rx together with NRC2 or NRC2^{D317K}, in the absence or
484 presence of SS15. C-terminally V5-tagged Rx and C-terminally 4xMyc-tagged NRC2^{EEE} or NRC2^{EEE-}

485 ^{D317K} were co-expressed with either free GFP or C-terminally GFP-tagged PVX CP. These effector-
486 sensor-helper combinations were co-infiltrated together with a 6xHA-mCherry fusion protein or with
487 N-terminally 4xHA-tagged SS15. Total protein extracts were run in parallel on native and denaturing
488 PAGE assays and immunoblotted with the appropriate antisera labelled below. Approximate
489 molecular weights (kDa) of the proteins are shown on the left. Corresponding SDS-PAGE blots can
490 be found in **Fig. S9**. The experiment was repeated three times with similar results.
491

492 **Supplemental Data**

493 **Figure S1**

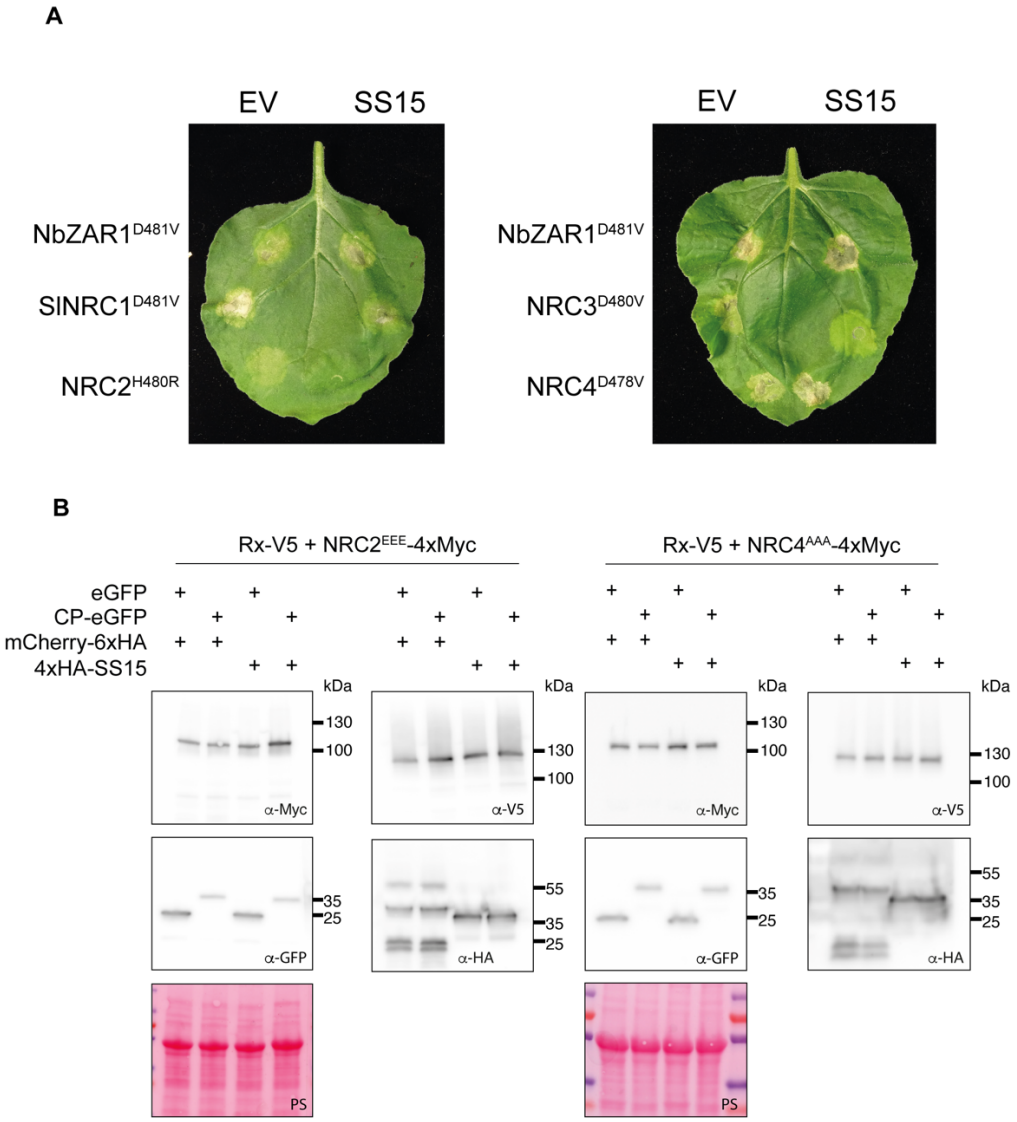

494

495 **Fig. S1: SS15 suppresses cell death mediated by SlNRC1, NRC2 and NRC3 but not NRC4 or**
496 **NbZAR1.**

497 (**A**) Photo of representative leaves from *N. benthamiana nrc2/3/4* KO plants showing HR after co-
498 expression of various autoactive NLR variants with a free mCherry-6xHA fusion protein (EV) or with
499 N-terminally 4xHA-tagged SS15. Images are representative of (**B**) SDS-PAGE accompanying BN-
500 PAGE shown in **Fig. 1B**. Total protein extracts were immunoblotted with the appropriate antisera
501 labelled on the left. Approximate molecular weights (kDa) of the proteins are shown on the right.
502 Rubisco loading control was carried out using Ponceau stain (PS). The experiment was repeated three
503 times with similar results.

504 # Figure S2

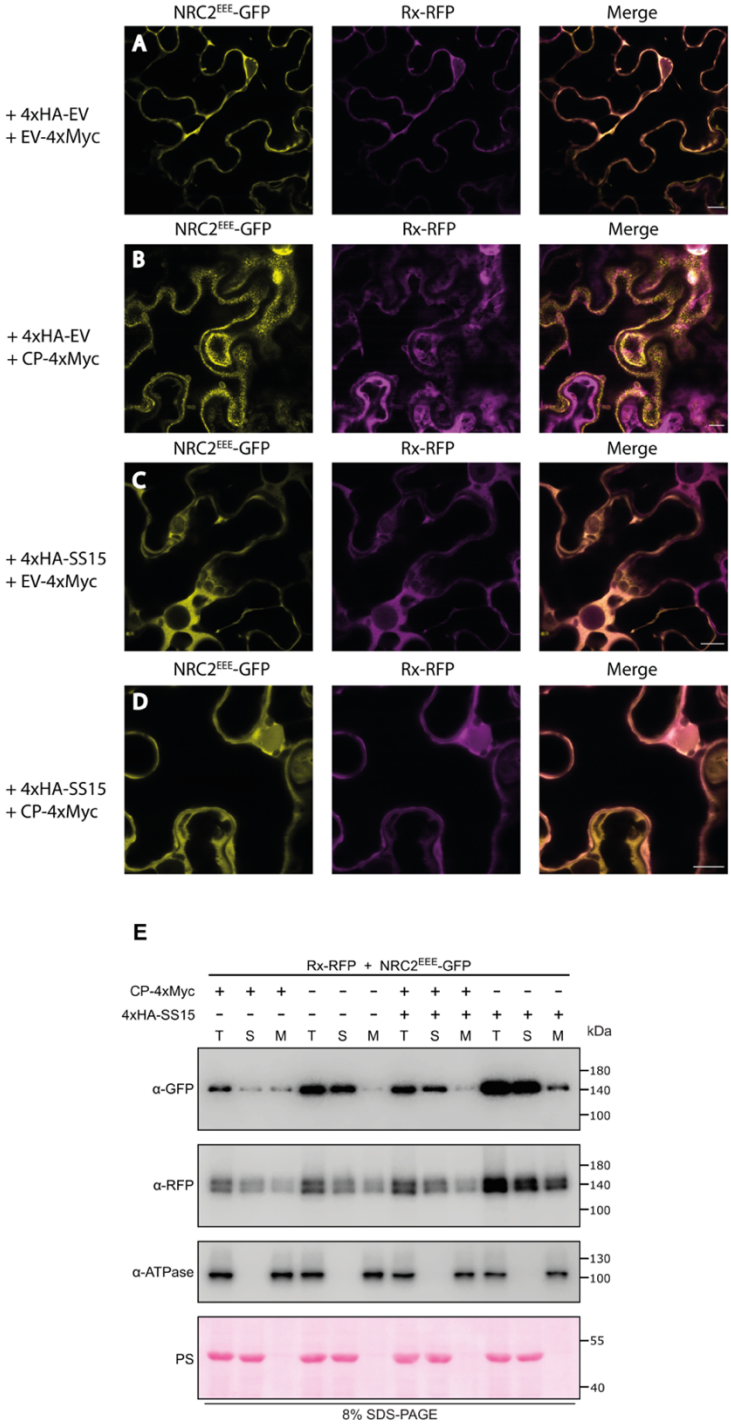

505

506 **Fig. S2: SS15 inhibits plasma membrane-association of activated NRC2.**

507 (**A-D**) C-terminally GFP-tagged NRC2^{EEE} and C-terminally RFP-tagged Rx were co-expressed with
508 an EV-4xMyc construct or a CP-4xMyc construct in leaves of *nrc2/3/4* KO *N. benthamiana*.
509 Representative single-plane confocal micrographs show the localization of both components of the

510 inactive and active Rx-NRC2 system. Scale bars represent 10 μm. (**A**) NRC2^{EEE}-GFP and Rx-RFP co-
511 localize in the cytoplasm. (**B**) As reported previously, Rx/CP activated NRC2^{EEE} forms plasma
512 membrane-associated puncta while Rx remains in the cytoplasm. (**C**) Co-expression with SS15 does
513 not alter the localization of inactive NRC2^{EEE}-GFP or Rx-RFP. (**D**) Upon co-expression CP-4xMyc,
514 Rx-RFP and NRC2^{EEE}-GFP with SS15, the punctate localization for NRC2^{EEE}-GFP is no longer
515 observed. (**E**) Membrane enrichment assays are consistent with microscopy. As reported previously,
516 inactive NRC2^{EEE}-GFP is mostly present in the soluble fraction (S) whereas activated NRC2^{EEE}-GFP
517 exhibits equal distribution across soluble and membrane (M) fractions. Upon co-expression with SS15,
518 NRC2^{EEE}-GFP distribution remains in the soluble fraction regardless of the presence or absence of
519 PVX CP. The experiment was repeated twice with similar results.
520

521 # Figure S3

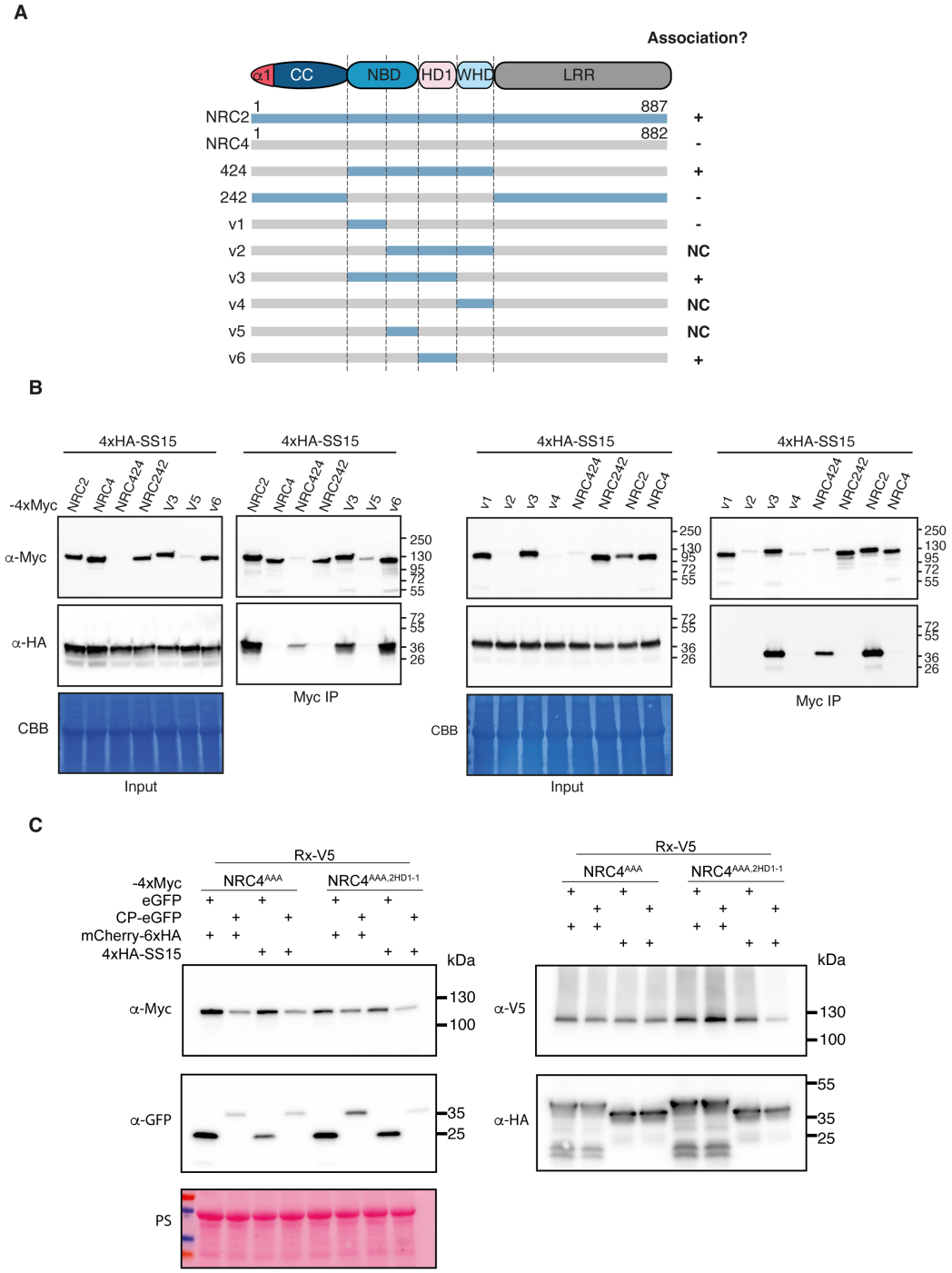

522

523 **Fig. S3: SS15 inhibits NRC2 by interacting with the HD1-1 region of the NB-ARC domain.**

524 **(A)** Schematic representation of all NRC2-NRC4 chimeric proteins generated. Association with SS15

525 (+) or lack thereof (-) is indicated on the right. (**B**) Co-Immunoprecipitation (Co-IP) assays between

526 SS15 and chimeric NRC2-NRC4 variants. C-terminally 4xMyc-tagged NRC proteins were transiently
527 co-expressed with N-terminally 4xHA-tagged SS15. IPs were performed with agarose beads
528 conjugated to Myc antibodies (Myc IP). Total protein extracts were immunoblotted with the
529 appropriate antisera labelled on the left. Approximate molecular weights (kDa) of the proteins are
530 shown on the right. Rubisco loading control was carried out using Ponceau stain (PS). The experiment
531 was repeated three times with similar results. (**C**) SDS-PAGE accompanying BN-PAGE shown in
532 **Fig. 2E**. Total protein extracts were immunoblotted with the appropriate antisera labelled on the left.
533 Approximate molecular weights (kDa) of the proteins are shown on the right. Rubisco loading control
534 was carried out using Ponceau stain (PS). The experiment was repeated three times with similar results.
535

536 # Figure S4

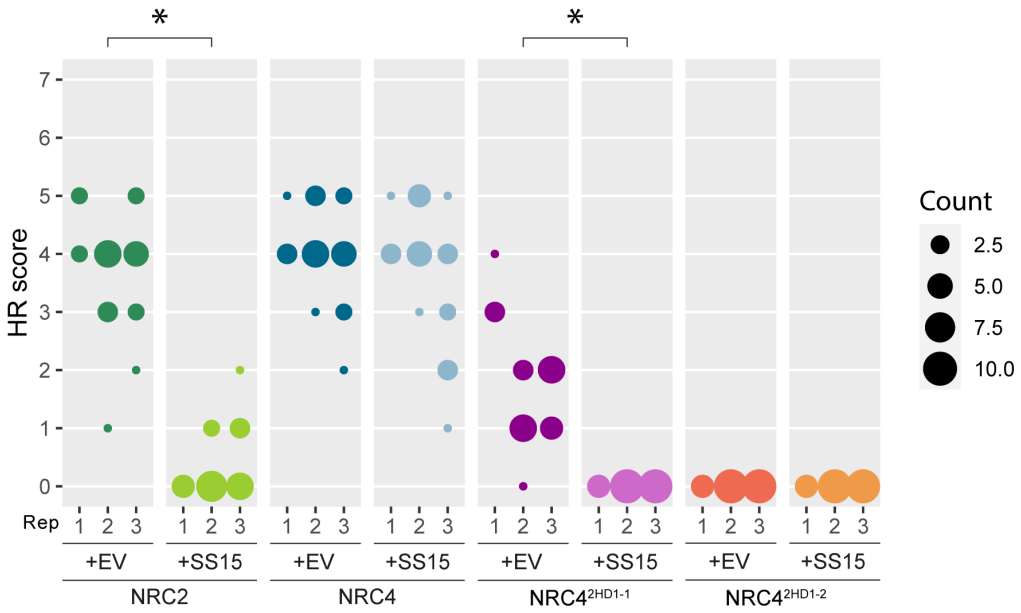

537

538 **Fig. S4: NRC4^{HD1-1} chimera is susceptible to inhibition by SS15.**

539 HR scores accompanying **Fig. 2D**. In all cases, Rx/CP was used to activate the system. HR was scored
540 based on a modified 0–7 scale (*49*) between 5–7 days post-infiltration. HR scores are presented as dot
541 plots, where the size of each dot is proportional to the number of samples with the same score (Count).
542 Results are based on 3 biological replicates. Statistical tests were implemented using the besthr R
543 library (*50*). We performed bootstrap resampling tests using a lower significance cut-off of 0.025 and
544 an upper cut-off of 0.975. Mean ranks of test samples falling outside of these cut-offs in the control
545 samples bootstrap population were considered significant. Significant differences between the
546 conditions are indicated with an asterisk (*).

547

548 **Figure S5**

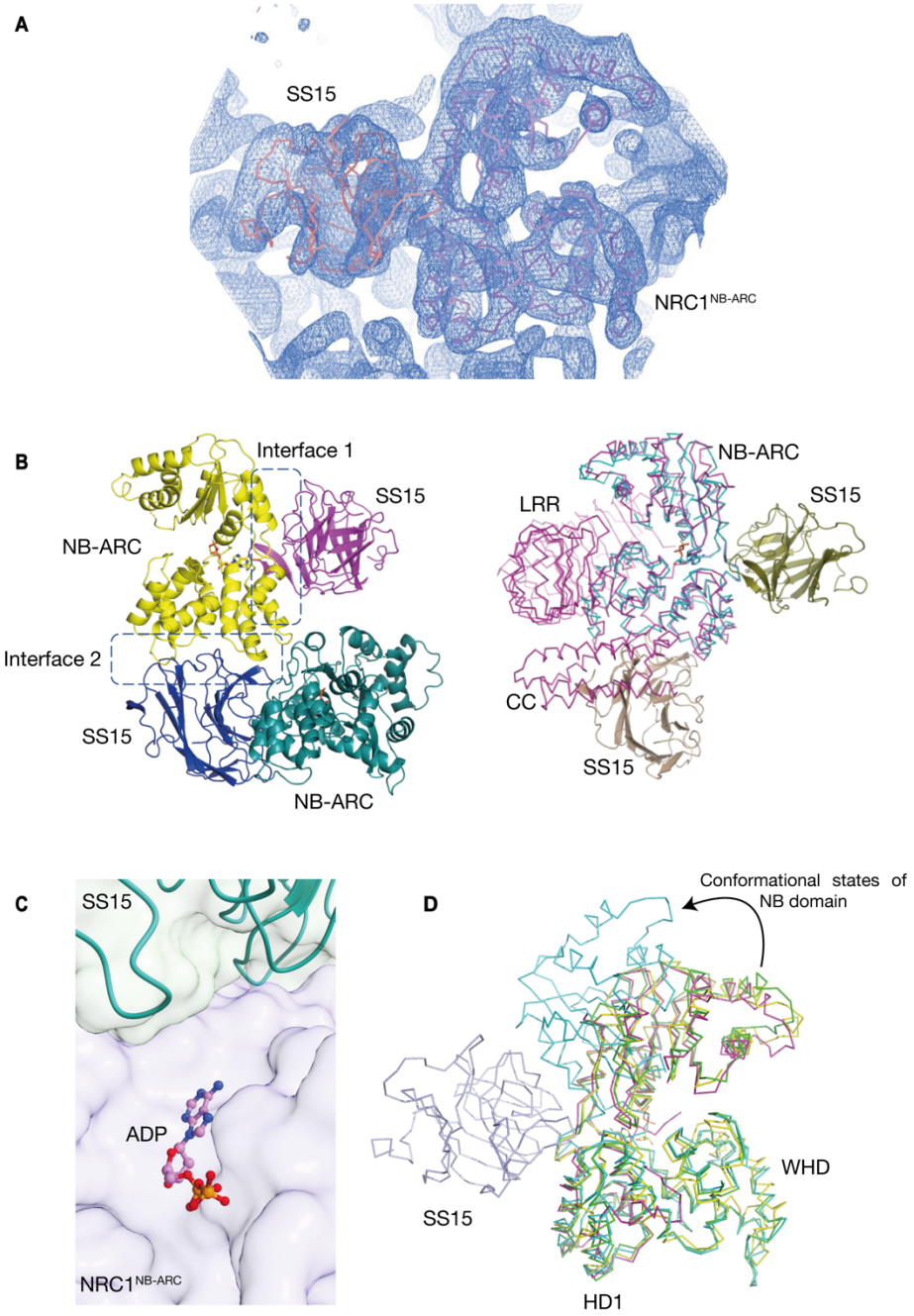

549

550 **Fig. S5: Crystal structure of SS15 in complex with SlNRC1$^{NB\text{-}ARC}$.**

551 Electron density map showing the relative orientation and arrangement of SS15 (orange) and
552 SlNRC1$^{NB\text{-}ARC}$ (violet) within an asymmetric unit. 2Fo-Fc map countered at 1σ **(B)** Two possible
553 interfaces between SS15 and SlNRC1$^{NB\text{-}ARC}$ revealed from the crystal packing. Both interfaces
554 (Interface 1 and Interface 2) are outlined (Left). Modelling of both potential binding interfaces for

555 SS15 complex with full length SlNRC1 (magenta) reveals a steric clash between the CC-domain of
556 SlNRC1 and SS15, making interface 2 unlikely to be biologically relevant in the full-length context
557 (Right). **(C)** Close up view of interaction between SS15-SlNRC1$^{NB\text{-}ARC}$ interaction interface relative to
558 the ATP-binding site within the NB-ARC domain of SlNRC1. The pyrophosphate moiety of ADP is
559 oriented facing opposite the SS15 binding interface (shown as ball and sticks), suggesting that SS15 is
560 unlikely to displace bound nucleotide or prevent ATP hydrolysis. **(D)** Structure of SS15-SlNRC1$^{NB\text{-}}$
561 ^{ARC} (yellow, PDB 8BV0) is superimposed over the NB-ARC domain of AtZAR1 in its inactive (green,
562 PDB 6J5W), intermediate (cyan, PDB 6J5V), and active resistosome (magenta, 6J5T) conformations.
563 Visualizing these three states reveals the trajectory of the NB domain as it moves relative to the HD1
564 and WHD domains while changing from inactive to activated states. The binding of SS15 at the critical
565 hinge region between the NB and HD1-WHD domains likely immobilizes this loop, preventing these
566 critical intramolecular rearrangements and therefore preventing NLR activation. See **Movie S1**.
567

568 **Figure S6**

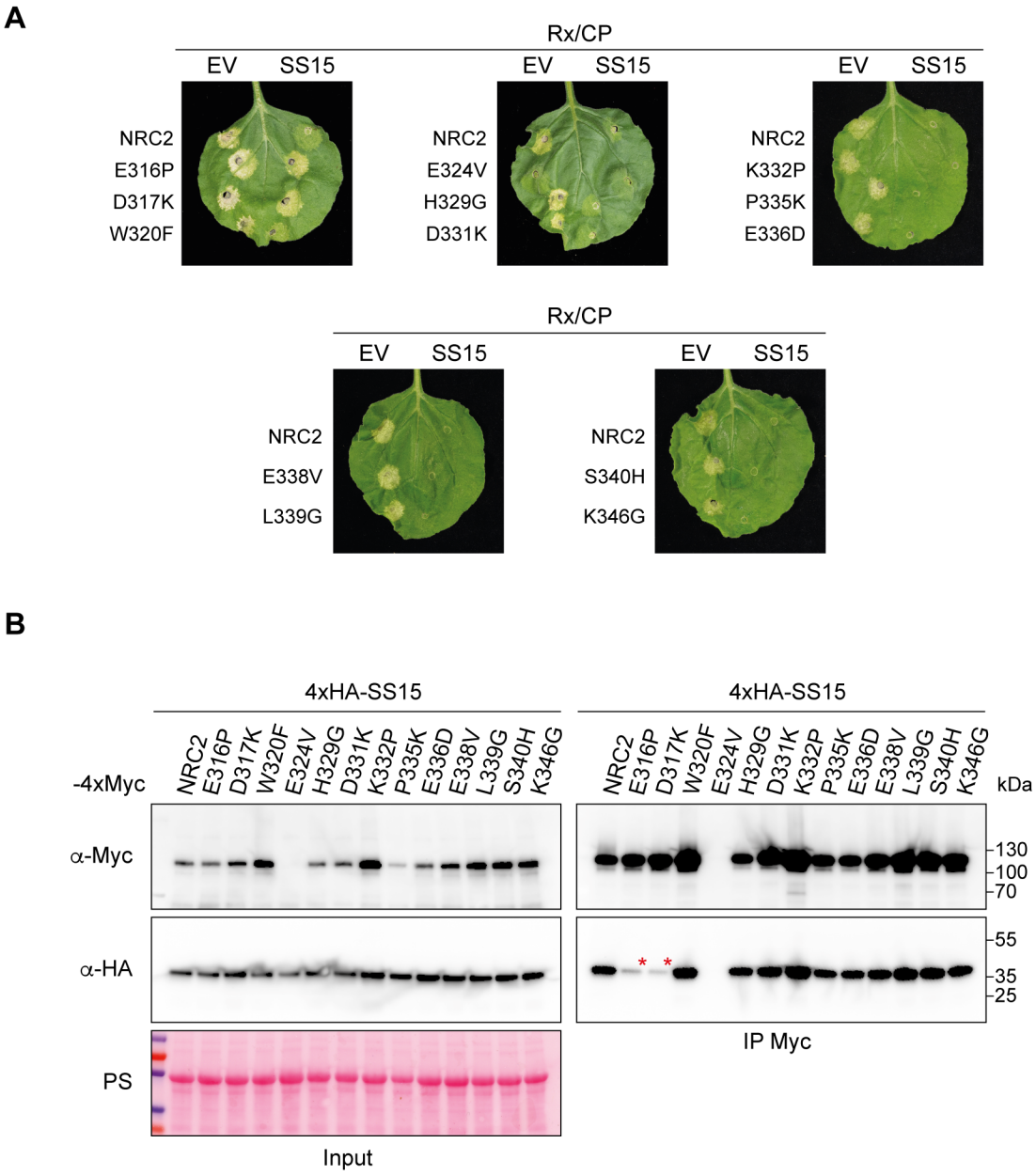

569

570

571 **Fig. S6: Out of 13 NRC2 variants tested, only E316P and D317K mutations abolish SS15**
572 **association and HR suppression. (A)** Photo of representative leaves from *N. benthamiana nrc2/3/4*
573 KO plants showing HR after co-expression of Rx and PVX CP with NRC2, or the different NRC2
574 variants generated. These effector-sensor-helper combinations were co-expressed with a free
575 mCherry-6xHA fusion protein (EV) or with N-terminally 4xHA-tagged SS15. (**B**) Co-
576 Immunoprecipitation (Co-IP) assays between SS15 and NRC2 variants. C-terminally 4xMyc-tagged

577 NRC2 variants were transiently co-expressed with N-terminally 4xHA-tagged SS15. IPs were
578 performed with agarose beads conjugated to Myc antibodies (Myc IP). Total protein extracts were
579 immunoblotted with appropriate antisera labelled on the left. Approximate molecular weights (kDa)
580 of the proteins are shown on the right. Rubisco loading control was carried out using Ponceau stain
581 (PS). The experiment was repeated three times with similar results.
582

583 # Figure S7

584

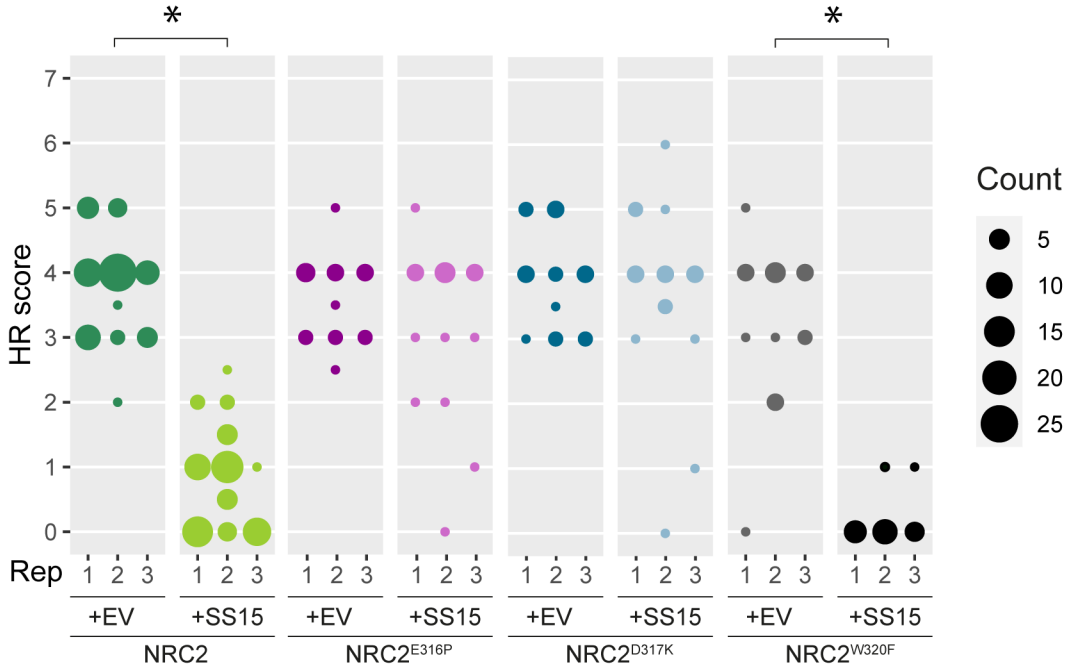

585

586 **Fig. S7: NRC2^{E316P} and NRC2^{D317K} abolish SS15-mediated suppression of Rx.**

587 HR scores accompanying **Fig. 3C**. In all cases, Rx/CP was used to activate the system. HR was scored
588 based on a modified 0–7 scale (*49*) between 5–7 days post-infiltration. HR scores are presented as dot
589 plots, where the size of each dot is proportional to the number of samples with the same score (Count).
590 Results are based on 3 biological replicates. Statistical tests were implemented using the besthr R
591 library (*50*). We performed bootstrap resampling tests using a lower significance cut-off of 0.025 and
592 an upper cut-off of 0.975. Mean ranks of test samples falling outside of these cut-offs in the control
593 samples bootstrap population were considered significant. Significant differences between the
594 conditions are indicated with an asterisk (*).

595

596 **Figure S8**

597

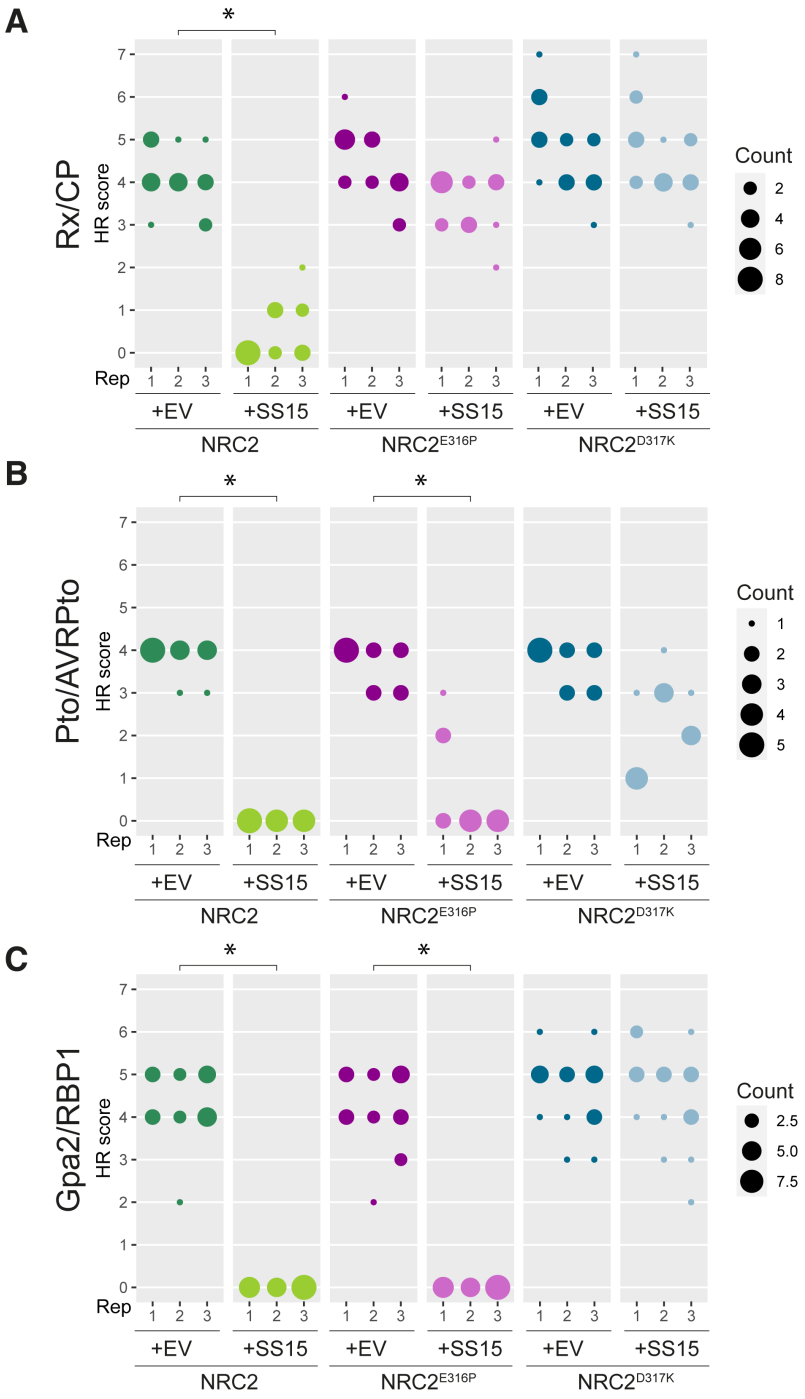

598

599 **Fig. S8: NRC2^{D317K} abolishes SS15-mediated suppression of Rx, Gpa2 and Prf.**

600 HR scores accompanying **Fig. 4A**. NRCs were activated using Rx/CP (**A**), Pto/AVRPto (**B**) or

601 Gpa2/RBP1 (**C**). HR was scored based on a modified 0–7 scale (*49*) between 5–7 days post-

infiltration. HR scores are presented as dot plots, where the size of each dot is proportional to the number of samples with the same score (count). Results are based on 3 biological replicates. Statistical tests were implemented using the besthr R library (*50*). We performed bootstrap resampling tests using a lower significance cut-off of 0.025 and an upper cut-off of 0.975. Mean ranks of test samples falling outside of these cut-offs in the control samples bootstrap population were considered significant. Significant differences between the conditions are indicated with an asterisk (*).

608 **Figure S9**

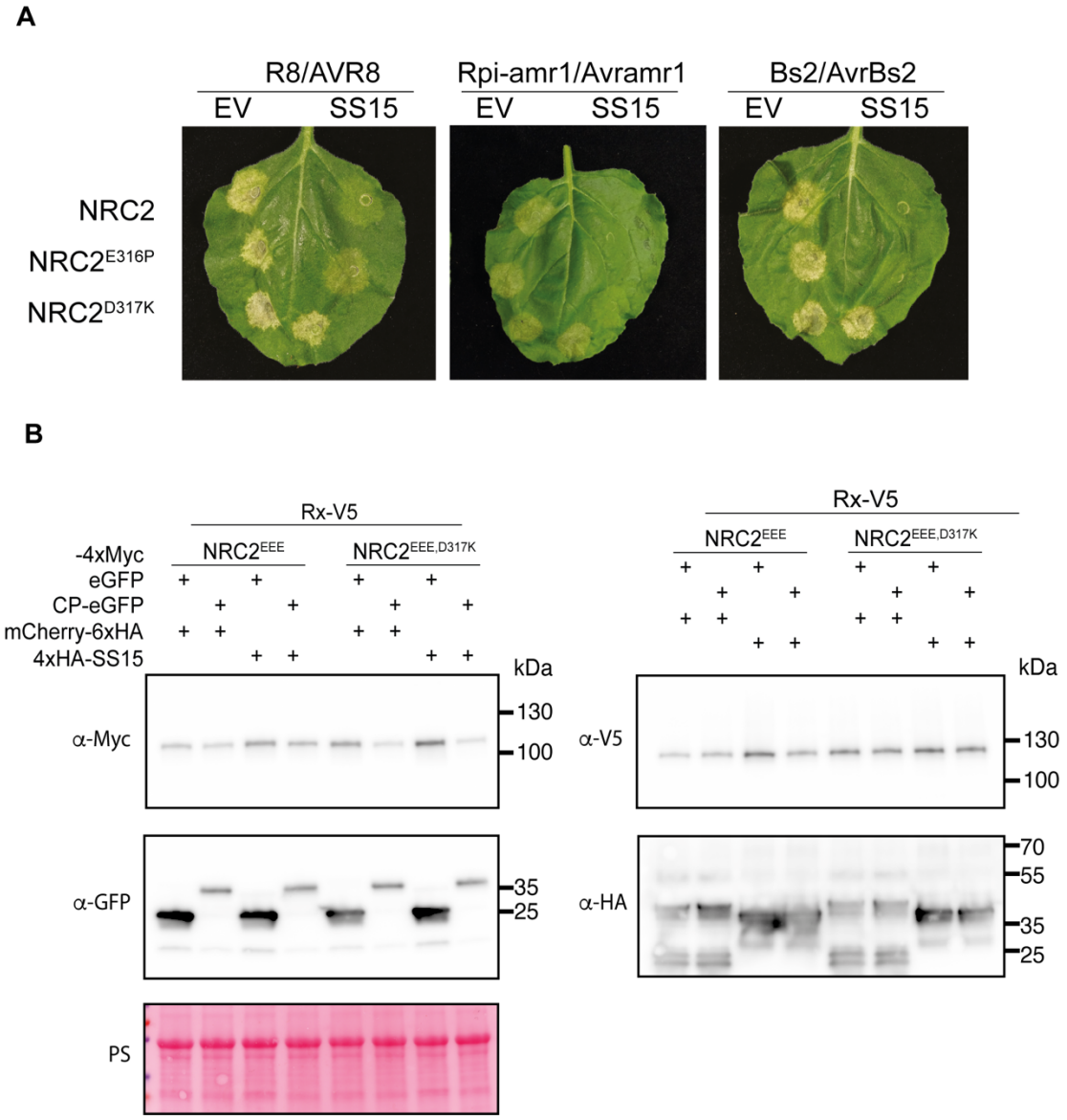

609

610 **Fig. S9: NRC2^{D317K} abolishes SS15-mediated suppression of all NRC2-dependent sensors**
611 **tested and restores NRC2 resistosome formation.**

612 Photo of representative leaves from *N. benthamiana nrc2/3/4* KO plants showing HR after co-
613 expression of NRC2, or different NRC2 variants generated with various sensor/effector pairs. These
614 effector-sensor-helper combinations were co-expressed with a free mCherry-6xHA fusion protein
615 (EV) or with N-terminally 4xHA-tagged SS15. (**B**) SDS-PAGE accompanying BN-PAGE shown in
616 **Fig. 4B**. Total protein extracts were immunoblotted with the appropriate antisera labelled on the left.
617 Approximate molecular weights (kDa) of the proteins are shown on the right. Rubisco loading control
618 was carried out using Ponceau stain (PS). The experiment was repeated three times with similar results.

619 ## Supplementary Tables

620 **Table S1: List of constructs used in this study.** (As separate file)

621 **Table S2: List of OD_{600} used for agroinfiltration experiments.** (As separate file)

622 **Table S3: Summary of X-ray data and model parameters for NRC1-SS15.**

623

Data collection	
Diamond Light Source beamline	I03
Wavelength (Å)	0.9763
Detector	Eiger2 XE 16M
Resolution range (Å)	51.34 – 4.50 (5.03 – 4.50)
Space Group	$P6_1$
Cell parameters (Å)	$a = b = 128.6$, $c = 170.7$
Total no. of measured intensities	77102 (13865)
Unique reflections	8981 (2263)
Multiplicity	8.6 (6.1)
Mean $I/\sigma(I)$	7.2 (1.5)
Completeness (%)	94.0 (84.0)
R_{merge}[a]	0.084 (1.513)
R_{meas}[b]	0.033 (0.612)
$CC_{½}$[c]	0.998 (0.588)
Refinement	
Resolution range (Å)	51.34 – 4.50 (4.62 – 4.50)
Reflections: working/free[d]	8075/883
R_{work}/ R_{free}[e]	0.237/0.275
MolProbity score/Clashscore[f]	1.58/5.41
Ramachandran plot: favoured/allowed/disallowed[f] (%)	95.9/4.1/0.0
R.m.s. bond distance deviation (Å)	0.003
R.m.s. bond angle deviation (°)	0.79
NRC1 – chains/no. protein residues/ranges	A,C/343/153-494
SS15 – chains/no. protein residues/ranges	B,D/206/18-223
No. ADP molecules/RSCC[g]	2/0.72,0.84

PDB accession code	8BV0

Values in parentheses are for the outer resolution shell.

[a] $R_{merge} = \sum_{hkl} \sum_{I} | I_i(hkl) - \langle I(hkl) \rangle | / \sum_{hkl} \sum_{i} I_i(hkl)$.

[b] $R_{meas} = \sum_{hkl} [N/(N-1)]^{1/2} \times \sum_{I} | I_i(hkl) - \langle I(hkl) \rangle | / \sum_{hkl} \sum_{i} I_i(hkl)$, where $I_i(hkl)$ is the ith observation of reflection hkl, $\langle I(hkl) \rangle$ is the weighted average intensity for all observations I of reflection hkl and N is the number of observations of reflection hkl.

[c] $CC_{½}$ is the correlation coefficient between symmetry equivalent intensities from random halves of the dataset.

[d] The data set was split into "working" and "free" sets consisting of 90 and 10% of the data respectively. The free set was not used for refinement.

[e] The R-factors R_{work} and R_{free} are calculated as follows: $R = \sum(| F_{obs} - F_{calc} |)/\sum| F_{obs} |$, where F_{obs} and F_{calc} are the observed and calculated structure factor amplitudes, respectively.

[f] As calculated using MolProbity (*51*).

[g] Real Space Correlation Coefficient as calculated by the PDB validation server.

Supplementary Movies

Movie S1: SS15 immobilizes hinge region between NB and HD1-WHD domains of NRCs to prevent NLR activation.

Acknowledgements

We are very thankful to Jiorgos Kourelis, Clemence Marchal, Daniel Lüdke and Hee-Kyung Ahn (The Sainsbury Laboratory, Norwich, UK) for invaluable scientific discussions, ideas, and feedback. We thank Julia Mundy for assistance with crystallography experiments. We thank the Diamond Light Source, UK (beamline i03 under proposal MX18565) for access to X-ray data collection facilities. M.P.C. thanks Emiliano "Dibu" Martínez and Lionel Messi for inspiration. We thank all members of the TSL Support Services for their invaluable assistance.

Funding:

The Kamoun Lab is funded primarily from the Gatsby Charitable Foundation, Biotechnology and Biological Sciences Research Council (BBSRC, UK, BB/WW002221/1, BB/V002937/1, BBS/E/J/000PR9795 and BBS/E/J/000PR9796) and the European Research Council (BLASTOFF).

Author Contributions:

Conceptualization: M.P.C, C-H.W., S.K., L.D.

Methodology: M.P.C., H.P., M.S., D.M.L., C.E.M.S., L.D.

Validation: M.P.C., H.P., M.S., Y.T., C.D., E.L.H.Y., A.H.

Formal Analysis: M.P.C., H.P., M.S., A.T., D.M.L., Y.T., C.D., C.E.M.S.

Investigation: M.P.C., H.P., M.S., Y.T., C.D., E.L.H.Y., A.H., L.D.

Data Curation: M.P.C., H.P., M.S., A.T., D.M.L., Y.T., C.D., E.L.H.Y., C.E.M.S., A.H.

Visualization: M.P.C., H.P., M.S., A.T., Y.T., C.D., E.L.H.Y., L.D.

Writing – Original Draft: M.P.C., S.K., L.D.

Writing – Review & Editing: M.P.C., D.M.L., S.K., L.D.

Supervision: M.P.C., T.O.B., S.K., L.D.

Project Administration: M.P.C., T.O.B., S.K., L.D.

Funding Acquisition: T.O.B., S.K., L.D.

Competing interests:

C.D., T.O.B and S.K. receive funding from industry on NLR biology. M.P.C., S.K. and L.D. have filed patents on NLR biology.

673 **Data and materials availability:**

674 All relevant data are within the paper, in the Supplementary Materials and Source Data files. Data
675 relevant to the structure presented in **Fig. 3** can be found in the Protein Data Bank, PDB 8BV0.

676

677 ## References

678

679 1. J. D. Jones, R. E. Vance, J. L. Dangl, Intracellular innate immune surveillance devices in
680 plants and animals. *Science* **354**, aaf6395 (2016).
681 2. Z. Duxbury, C.-h. Wu, P. Ding, A comparative overview of the intracellular guardians of
682 plants and animals: NLRs in innate immunity and beyond. *Annual review of plant biology*
683 **72**, 155-184 (2021).
684 3. J. Wang *et al.*, Reconstitution and structure of a plant NLR resistosome conferring
685 immunity. *Science* **364**, eaav5870 (2019).
686 4. M. P. Contreras *et al.*, Sensor NLR immune proteins activate oligomerization of their NRC
687 helper. *The EMBO Journal, in press* (2022).
688 5. H.-K. Ahn *et al.*, Effector-dependent activation and oligomerization of NRC helper NLRs by
689 Rpi-amr3 and Rpi-amr1. *The EMBO Journal, in press* (2022).
690 6. A. Förderer *et al.*, A wheat resistosome defines common principles of immune receptor
691 channels. *bioRxiv*, 2022.2003.2023.485489 (2022).
692 7. R. Martin *et al.*, Structure of the activated ROQ1 resistosome directly recognizing the
693 pathogen effector XopQ. *Science* **370**, eabd9993 (2020).
694 8. I. V. Hochheiser *et al.*, Structure of the NLRP3 decamer bound to the cytokine release
695 inhibitor CRID3. *Nature* **604**, 184-189 (2022).
696 9. Z. Hu *et al.*, Structural and biochemical basis for induced self-propagation of NLRC4.
697 *Science* **350**, 399-404 (2015).
698 10. Z. Duxbury *et al.*, Induced proximity of a TIR signaling domain on a plant-mammalian NLR
699 chimera activates defense in plants. *Proceedings of the National Academy of Sciences* **117**,
700 18832-18839 (2020).
701 11. B. P. M. Ngou, P. Ding, J. D. Jones, Thirty years of resistance: Zig-zag through the plant
702 immune system. *The Plant Cell* **34**, 1447-1478 (2022).
703 12. L. A. Gao *et al.*, Prokaryotic innate immunity through pattern recognition of conserved
704 viral proteins. *Science* **377**, eabm4096 (2022).
705 13. C.-H. Wu, L. Derevnina, S. Kamoun, Receptor networks underpin plant immunity. *Science*
706 **360**, 1300-1301 (2018).
707 14. L. D. Cunha *et al.*, Inhibition of inflammasome activation by Coxiella burnetii type IV
708 secretion system effector IcaA. *Nature communications* **6**, 1-13 (2015).
709 15. L. Derevnina *et al.*, Plant pathogens convergently evolved to counteract redundant nodes
710 of an NLR immune receptor network. *PLoS biology* **19**, e3001136 (2021).
711 16. H. Yen, N. Sugimoto, T. Tobe, Enteropathogenic Escherichia coli uses NleA to inhibit NLRP3
712 inflammasome activation. *PLoS pathogens* **11**, e1005121 (2015).
713 17. Q. Chai *et al.*, A bacterial phospholipid phosphatase inhibits host pyroptosis by hijacking
714 ubiquitin. *Science* **378**, eabq0132 (2022).

715 18. C. Marchal, H. Pai, S. Kamoun, J. Kourelis, Emerging principles in the design of
716 bioengineered made-to-order plant immune receptors. *Current Opinion in Plant Biology*,
717 102311 (2022).
718 19. J. Kourelis, T. Sakai, H. Adachi, S. Kamoun, RefPlantNLR is a comprehensive collection of
719 experimentally validated plant disease resistance proteins from the NLR family. *PLoS*
720 *Biology* **19**, e3001124 (2021).
721 20. H. Adachi, L. Derevnina, S. Kamoun, NLR singletons, pairs, and networks: evolution,
722 assembly, and regulation of the intracellular immunoreceptor circuitry of plants. *Current*
723 *opinion in plant biology* **50**, 121-131 (2019).
724 21. C.-H. Wu *et al.*, NLR network mediates immunity to diverse plant pathogens. *Proceedings*
725 *of the National Academy of Sciences* **114**, 8113-8118 (2017).
726 22. C. N. LaRock, B. T. Cookson, The Yersinia virulence effector YopM binds caspase-1 to arrest
727 inflammasome assembly and processing. *Cell host & microbe* **12**, 799-805 (2012).
728 23. H. Chen *et al.*, The bacterial T6SS effector EvpP prevents NLRP3 inflammasome activation
729 by inhibiting the Ca2+-dependent MAPK-Jnk pathway. *Cell host & microbe* **21**, 47-58
730 (2017).
731 24. H. S. Karki, S. Abdullah, Y. Chen, D. A. Halterman, Natural genetic diversity in the potato
732 resistance gene RB confers suppression avoidance from Phytophthora effector IPI-O4.
733 *Molecular Plant-Microbe Interactions* **34**, 1048-1056 (2021).
734 25. H. Adachi *et al.*, An N-terminal motif in NLR immune receptors is functionally conserved
735 across distantly related plant species. *Elife* **8**, e49956 (2019).
736 26. J. Kourelis *et al.*, The helper NLR immune protein NRC3 mediates the hypersensitive cell
737 death caused by the cell-surface receptor Cf-4. *bioRxiv*, (2021).
738 27. J. Wang *et al.*, Ligand-triggered allosteric ADP release primes a plant NLR complex. *Science*
739 **364**, eaav5868 (2019).
740 28. J. Kourelis, C. Marchal, S. Kamoun, NLR immune receptor-nanobody fusions confer plant
741 disease resistance. *bioRxiv*, (2021).
742 29. E. Weber, C. Engler, R. Gruetzner, S. Werner, S. Marillonnet, A modular cloning system for
743 standardized assembly of multigene constructs. *PloS one* **6**, e16765 (2011).
744 30. C. Engler *et al.*, A golden gate modular cloning toolbox for plants. *ACS synthetic biology* **3**,
745 839-843 (2014).
746 31. M. P. Contreras *et al.*, Sensor NLR immune proteins activate oligomerization of their NRC
747 helper. *BioRxiV*, (2022).
748 32. L. Derevnina *et al.*, Plant pathogens convergently evolved to counteract redundant nodes
749 of an NLR immune receptor network. *PLoS biology* **19**, e3001136 (2021).
750 33. C. Duggan *et al.*, Dynamic localization of a helper NLR at the plant–pathogen interface
751 underpins pathogen recognition. *Proceedings of the National Academy of Sciences* **118**,
752 (2021).
753 34. L. Abas, C. Luschnig, Maximum yields of microsomal-type membranes from small amounts
754 of plant material without requiring ultracentrifugation. *Analytical biochemistry* **401**, 217-
755 227 (2010).
756 35. F. W. Studier, Protein production by auto-induction in high-density shaking cultures.
757 *Protein expression and purification* **41**, 207-234 (2005).

36. J. F. Steele, R. K. Hughes, M. J. Banfield, Structural and biochemical studies of an NB-ARC domain from a plant NLR immune receptor. *PLoS One* **14**, e0221226 (2019).
37. W. Kabsch, xds. *Acta Crystallographica Section D: Biological Crystallography* **66**, 125-132 (2010).
38. G. Winter, xia2: an expert system for macromolecular crystallography data reduction. *Journal of applied crystallography* **43**, 186-190 (2010).
39. P. R. Evans, G. N. Murshudov, How good are my data and what is the resolution? *Acta Crystallographica Section D: Biological Crystallography* **69**, 1204-1214 (2013).
40. M. Winn, An overview of the CCP4 project in protein crystallography: an example of a collaborative project. *Journal of synchrotron radiation* **10**, 23-25 (2003).
41. R. Evans *et al.*, Protein complex prediction with AlphaFold-Multimer. *bioRxiv*, 2021.2010.2004.463034 (2022).
42. M. Mirdita *et al.*, ColabFold: making protein folding accessible to all. *Nature Methods*, 1-4 (2022).
43. A. J. McCoy *et al.*, Phaser crystallographic software. *Journal of applied crystallography* **40**, 658-674 (2007).
44. P. Emsley, B. Lohkamp, W. G. Scott, K. Cowtan, Features and development of Coot. *Acta Crystallographica Section D: Biological Crystallography* **66**, 486-501 (2010).
45. G. N. Murshudov *et al.*, REFMAC5 for the refinement of macromolecular crystal structures. *Acta Crystallographica Section D: Biological Crystallography* **67**, 355-367 (2011).
46. R. A. Nicholls, M. Fischer, S. McNicholas, G. N. Murshudov, Conformation-independent structural comparison of macromolecules with ProSMART. *Acta Crystallographica Section D: Biological Crystallography* **70**, 2487-2499 (2014).
47. E. F. Pettersen *et al.*, UCSF ChimeraX: Structure visualization for researchers, educators, and developers. *Protein Science* **30**, 70-82 (2021).
48. The PyMOL Molecular Graphics System, Version 1.2r3pre, Schrödinger, LLC.
49. M. E. Segretin *et al.*, Single amino acid mutations in the potato immune receptor R3a expand response to Phytophthora effectors. *Molecular Plant-Microbe Interactions* **27**, 624-637 (2014).
50. D. MacLean, Besthr. *Zenodo*, (2019).
51. I. W. Davis *et al.*, MolProbity: all-atom contacts and structure validation for proteins and nucleic acids. *Nucleic acids research* **35**, W375-W383 (2007).